A Device for Measuring the Wire Tension of the MWPCs in the CBM TRD

Bachelor thesis
submitted to the

Universität Münster
Institut für Kernphysik

by
Johannes Lämmel

April 2024

First examiner:	Prof. Dr. Anton Andronic
Second examiner:	Apl. Prof. Dr. Christian Klein-Bösing
Day of submission:	Friday 26th April, 2024

Affidativ of Academic Integrity

I, Johannes Lämmel, hereby declare that I have written this thesis independently, affirming that it is solely my own work. I have not utilized any sources or aids beyond those explicitly stated. All content, including ideas, wording, and references, has been substantiated or acknowledged appropriately. All passages in my thesis for which sources, including electronic media, have been used, be it direct quotes or content references, have been acknowledged as such and the sources cited. This encompasses any external materials such as images, tables, or drawings, which have been properly attributed. I am aware that plagiarism is considered an act of deception, which will result in sanction in accordance with the examination regulations.

Münster, 26th April 2024

Johannes Lämmel

I consent to having my thesis cross-checked with other texts to identify possible similarities and to having it stored in a database for this purpose. I confirm that I have not submitted the following thesis in part or whole as an examination paper before.

Contents

1 Introduction

The exploration of fundamental particles and their interactions is an important subject of modern physics, driving our understanding of the universe's most fundamental processes. Among the numerous experiments seeking to unravel these mysteries, the investigations of extraordinary states of matter, like the Quark-Gluon Plasma (QGP) are exciting endeavors. Within this context, the need for large-scale experiments becomes evident, as the necessary conditions for creating such matter state probes are far beyond normal scale. Additionally, the development and deployment of sophisticated detection systems are crucial, as they provide the necessary tools for probing deep into the fundamental laws of nature.

This thesis contributes to the ongoing research efforts of the CBM (Compressed Baryonic Matter) experiment, which is dedicated to the study of the QCD phase diagram. Situated at the future particle accelerator SIS100 within the Facility for Antiproton and Ion Research (FAIR) in Darmstadt, Germany, CBM represents a collaborative initiative aimed at unlocking the secrets of strongly interacting matter.

In particular, this thesis focuses on the mechanical tension of the wires in the Multi Wire Proportional Chambers (MWPCs) of the Transition Radiation Detector (TRD) within this experimental collaboration. During the production process of the detector modules, the tension with which the wires that serve as electrodes should be monitored. The aim of this work is to present the concept for a device that reliably both locates the wires within these chambers and measures their mechanical tension.

2 Experimental Background

FAIR

The international accelerator facility FAIR is currently under construction based upon an expansion of the GSI Helmholtz Centre for Heavy Ion Research (German: "Gesellschaft für Schwerionenforschung") in Darmstadt. Research will take place regarding the four scientific pillars of FAIR: Atomic, Plasma Physics, and Applications (APPA); Compressed Baryonic Matter (CBM); Nuclear Structure, Astrophysics, and Reactions (NUSTAR); and Anti*p*roton *An*nihilation at *Da*rmstadt ($\bar{\text{P}}$ANDA).

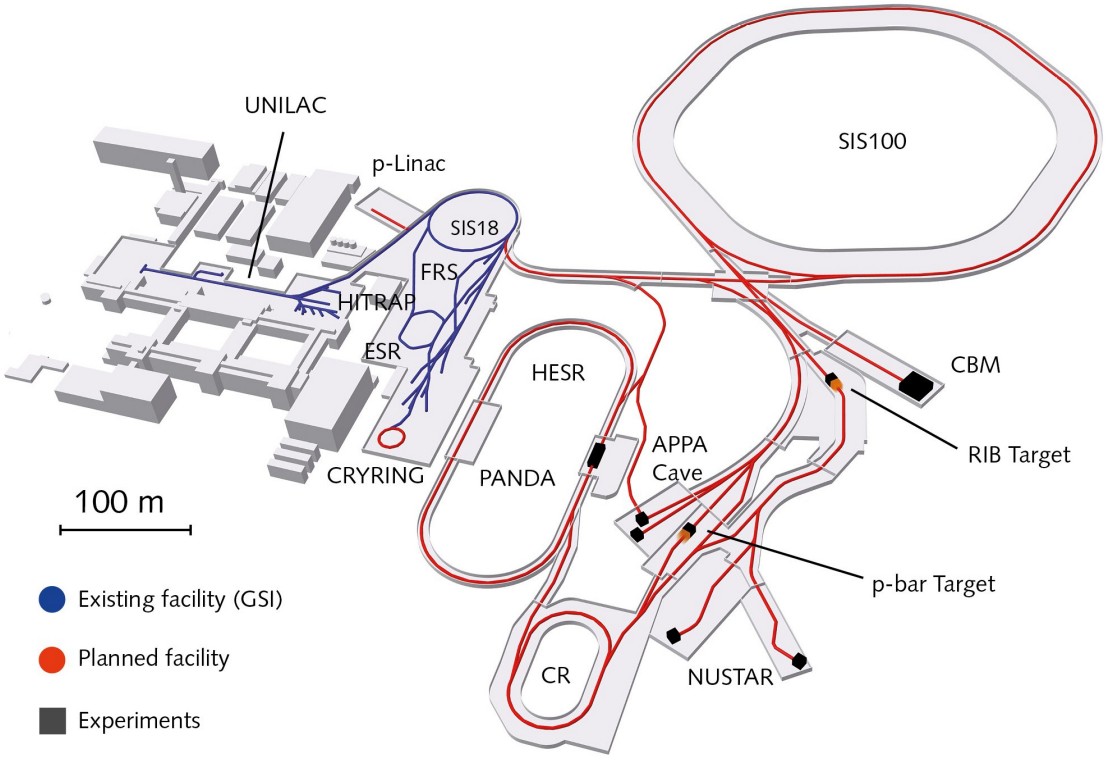

Figure 2.1: Planned layout of the future Facility for Antiproton and Ion Research (FAIR) including its experiments [TDR18].

In the future, when the entire facility is operational, the heavy ions required for experiments will be prepared in the UNILAC linear accelerator. Subsequently, they

will be injected into the SIS18 synchrotron for pre-acceleration before being further accelerated to their final kinetic energy in the SIS100, as shown in figure 2.1. From there, the ion beam will be directed to the specific experiments, such as CBM [Gut06].

The heart of FAIR, the ring accelerator SIS100, derives its name (with "SIS" being the acronym for the German term "Schwerionensynchrotron", meaning heavy ion synchrotron) from its bending power, or beam rigidity, of $R = 100\,\mathrm{T\,m}$ [Gut06]. The SIS100 with a circumference of $1084\,\mathrm{m}$ is designed to accommodate a wide range of ions, from protons to uranium. Notably, it is capable of achieving energy levels that are 20 times higher, and beam intensities that are ten orders of magnitude greater than what was possible at GSI so far [Gut06].

CBM Experiment

The CBM (Compressed Baryonic Matter) experiment is a novel initiative designed to explore the fundamental properties of nuclear matter at extreme densities. To accomplish this, the experiment will investigate the phase diagram of strongly interacting matter through high-energy nucleus-nucleus collisions. This diagram, also known as the QCD phase diagram, is shown in figure 2.2 and based on Quantum Chromodynamics (QCD), which describes the strong interaction.

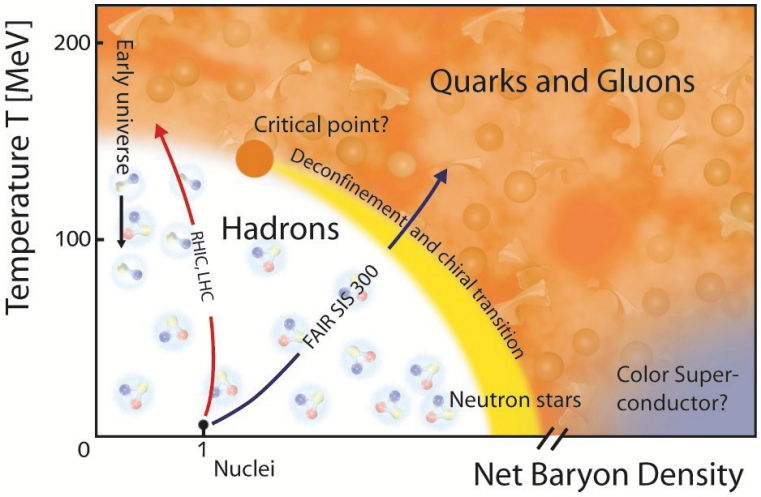

Figure 2.2: Phase diagram of strongly interacting matter in a schematic representation with temperature versus net-baryon density [Gut06].

The "normal" nuclear matter, as found inside of large atomic nuclei, can be found in this diagram at low temperatures and a net baryon density of one. The nucleons, proton and neutron, forming an atomic nucleus, are baryons because they contain an odd number of valence quarks. These quarks are one of the fundamental particles of the standard model of particle physics. All composite subatomic particles containing quarks and antiquarks, are called hadrons. The quarks are bound by

the strong interaction mediated by particles called the gluons [DF03].
At higher temperatures or baryon densities the hadrons sort of "melt" to the Quark-Gluon Plasma. Here the color charged particles, meaning quarks, antiquarks and gluons, can move around the whole volume of the QGP, just as it is known from the plasma as a state of ordinary matter [Fri11].

Other collider experiments focus on the QGP at high temperatures, since it is assumed to have existed shortly after the Big Bang. A Large Ion Collider Experiment (ALICE) at the Large Hadron Collider (LHC) should be mentioned here in particular, as it also provides a basis for this thesis.
However, in regards to the CBM experiment at FAIR the focus is not high temperature but rather on whether matter at high baryon densities disintegrates into its elementary particles forming QGP. Such high densities may be found in the core of a neutron star [Fri11].

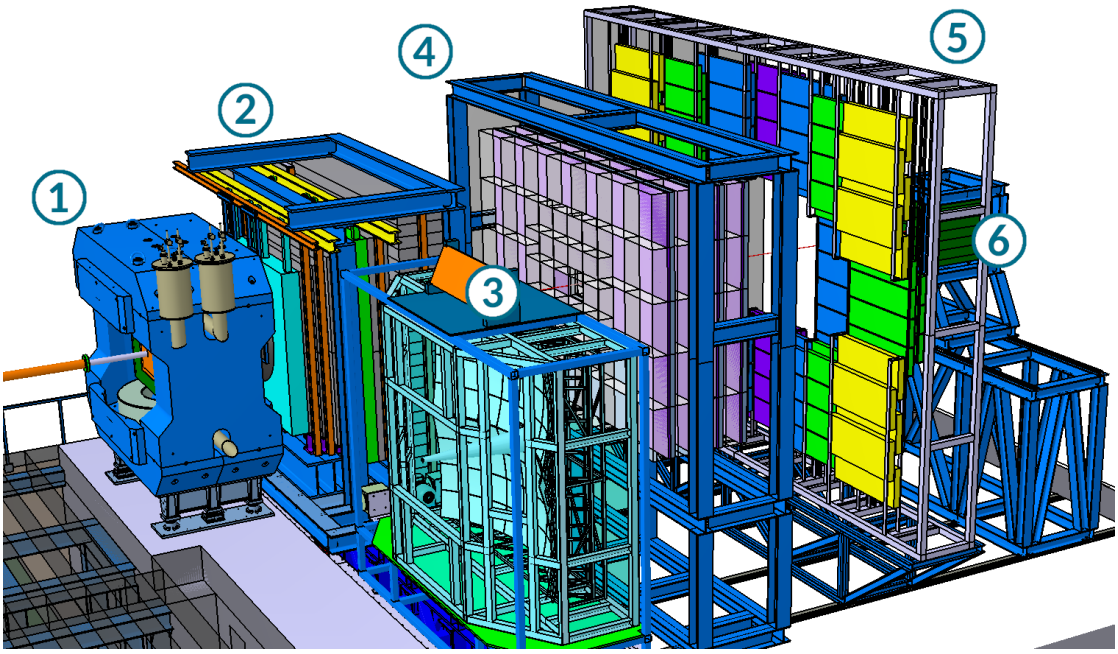

Figure 2.3: Schematic view of the CBM detectors [TDR18]. Since the particles propagate in a cone shape in the direction of the beam from the vertex, each wall-like detector layer must cover a larger area the further it is from the target.

These high densities are created on a very small scale using the collision of the accelerated heavy ion beam on a fixed target. This collision forms a high-density *fireball* which has a too short existence to be studied directly. So the CBM experiment has to instead focus on the secondary particles, which are created in consequence of the collision. [Fri11].
Only a few $10^{-23}\,\mathrm{s}$ are needed from the collision for the particles to "freeze out"

back into hadrons. Therefore, the CBM experiment is intended to run with reaction rates of up to $10\,\mathrm{MHz}$, in order to achieve high statistics data [Gut06]. Resulting in multiplicities of up to 1000 charged particles per nucleus-nucleus collision event, the CBM experiment requires unparalleled, radiation-resistant detector capabilities as well as fast data acquisition, transmission and computing technology.

The individual detectors that together comprise the CBM experiment as shown in figure 2.3 are the following [TDR18]:

1 Dipole Magnet to deflect the charged particles produced during the collision.

Within 1: Target As the CBM experiment is a fixed target collision experiment, the particle beam at this point hits a foil which serves as the target.

Within 1: Micor-Vertex Detector (MVD) to reconstruct the location of the initial and secondary vertices with four layers of Monolithic Active Pixel Sensors (MAPS).

Within 1: Silicon Tracking System (STS) to track and determine the momentum of each particle with with eight layers of spatially resolving silicon strip detectors.

2 Muon Chamber System (MUCH) to track Muons through a hadron absorber with several iron plates alternating with gaseous tracking chambers. For this is stopping almost all particles except the muons, just the first layers of the TRD but no further detectors are used in the muon detection setup.

3 Ring Imaging Cherenkov Detector (RICH) In the electron-hadron setup MUCH is replaced by the RICH detector. The rings of the Cherenkov light from electrons and positrons inside the medium are captured with two arrays of mirrors and photon detector planes.

4 Transition Radiation Detector The detector, to which this thesis contributes, uses Transition Radiation (TR) to distinguish mainly between pions and electrons, making it possible to identify electrons and positrons with higher momenta.

5 Time-Of-Flight System (TOF) to determine the speed of the particles by taking the time for traveling from the vertex to the TOF-Wall with an array of Multi-gap Resistive Plate Chambers (MRPC).

6 Fragment Spectator Detector (FSD) to determine the angle of the collision plane and the centrality, by measuring the number of the non-interacting nucleons ("spectators") from the ion beam.

Together with the SIS100 accelerator, which delivers high-intensity heavy-ion beams, the conjunction of these detectors enables the acquisition of precise information from the collision and the resulting fireball of compressed baryonic matter.

3 Detector Principle

The CBM Transition Radiation detector consists of Multi-Wire Proportional Chambers (MWPCs) to detect particle tracks and radiation caused by the transition of a charged particle from one medium to another. In the following, the underlying principle of gas-filled radiation detectors will be explained.

3.1 Gas-filled Radiation Detectors

When ionizing particles pass through a gas medium, they can transfer energy to the atoms in the gas. This transfer of energy can be sufficient to remove one or more electrons from the atoms, thereby creating ions. The radiation can consist of charged particles, whose energy lost in the medium can be calculated with the *Bethe–Bloch formula*. Also electromagnetic radiation leads to ionization via the *photoelectric effect*, *compton scattering* or *pair production*, depending on the energy of the incident rays [Gru93].
If the ionization occurs in an electric field the electrons and ions produced are separated, preventing them from recombining and allowing for detection.

Ionization Chamber With this basic principle of placing a gas volume inside an electric field, generated by two electrodes, similar to a capacitor, the *ionization chamber*, is created. It is not sensitive to single particles, because the lower detection limit is around $q = 1\,\mathrm{fC} \approx 10^4 \cdot e$. Additionally current measurements can only begin in the pA to nA range, with $1\,\mathrm{nA} = 1\,{}^{\mathrm{nC}}/_{\mathrm{s}}$ already corresponding to 10^{10} ionizations [KW16].

Counter Tube Given these limitations, the number of charges resulting from one particle ionizing the gas must be amplified in order to detect a single particle. This leads to the "Wire-Cylinder Ionization Detection System". It resembles a cylindrical capacitor with the rim of the cylinder acting as cathode and a wire in the center

of the tube as anode. Because the electric field of this setup is rising the closer it is to the center ($E \sim 1/r$) the electrons created by the ionization are accelerated on their way towards the anode wire. Having acquired sufficient kinetic energy, they can ionize gas atoms on their own (secondary ionization). The electrons created in this process are accelerated again, thus also initiating ionization. This leads to a cascading process, giving rise to an avalanche of charges. In this way, each incoming particle is triggering a cascade of charges which amplifies the initial charge by a factor G of 10^4 to 10^6, called the *gas gain* [KW16]. This makes it possible to count each incident particle, which is why this system is also called *counter tube*.

Proportional Counters With a constant gas gain the amplified charge is proportional to the initial charge, but now big enough to be measured. Furthermore the gas gain G (for one voltage) is always the same and does not depend on the primary ionization. In this way radiation of different energies can be distinguished in *proportional counters*, because an incident particle or ray with higher energy will have more primary ionization events along its track through the gas.

The Transition Radiation detector of the CBM experiment, consists of Multi-Wire Proportional Chambers (MWPCs). As the name depicts they use the principle of proportional counters, but additionally have a spatial resolution. How this is achieved is discussed in the following section.

3.1.1 Multi-Wire Proportional Chambers

The simplest way to achieve a spatial resolution is to just put several counter tubes side by side, as shown in figure 3.1.

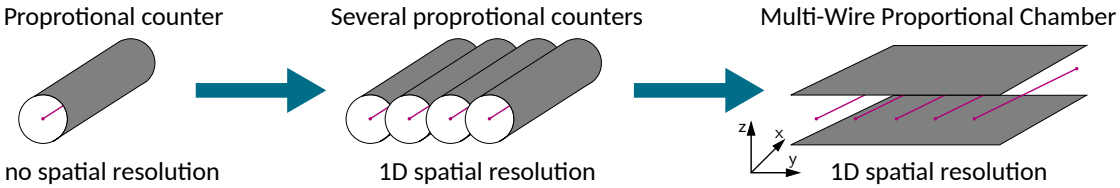

Figure 3.1: To achieve a spatial resolution in one dimension in the simplest way proportional counters can be used next to each other. If the cathode walls are removed and two plates are used instead, the result is a MWPC.

Conveniently, it does not require a separation between the anode wires to obtain signals from individual wires without cross-talk, thereby requiring less interfering material.

Typically the space between the wires $\Delta y = p$ is smaller than the space between the wires and the cathodes $\Delta z = h$ [KW16][1].

So far the track of the radiation going through the chamber can be resolved along one axis rectangular to the wires (y-direction). In order to achieve a spatial resolution in a second dimension, the MWPC setup can be changed. Adding rotated anode wire planes is possible, but the MWPCs of the CBM TRD use another method, the cathode read-out.
These utilize the induced charge signal on the cathode. This electrostatic induction can be exemplified by the *method of mirrored charges*: Once the electrons reach the anode their charge is mirrored or induced to the cathodes. If the cathode plane is now separated crosswise to the anode wires the second spatial coordinate can be achieved.

To reduce readout effort in the CBM TRD, just the signal on the cathodes is used. Therefore the cathodes are not just divided into strips but also into pads in order to achieve a granular resolution with two spatial coordinates.
The distribution of the induced charges on the pads in one direction is calculated semi-empirically according to Mathieson [Mat88], resulting in a in a Gaussian-like Pad Response Function (PRF).
The MWPC geometry in CBM TRD is configured in such a manner that, approximately 80% of the charge from a central hit is detected in the affected pad, and 10% each on the adjoining pads.
Thereby, a resolution can be achieved that is many times higher than the actual pad width [Gru93]. In the CBM TRD with a pad width of $6.7\,\mathrm{mm}$ a spatial resolution in y-direction of $300\,\mu\mathrm{m}$ to $400\,\mu\mathrm{m}$ is realized [TDR18][PK20].

[1] Remark on the coordinate system used in this work: The direction along the wires is always the x-direction and the second coordinate which spans the wire plane is the y-direction. The linear drive of the measuring device presented here also moves along this axis. Finally, the z-axis runs vertically on the wire plane in the original beam direction.

3.2 Transition Radiation Detectors

Transition Radiation refers to the electromagnetic radiation emitted when a charged particle traverses the boundary between two media with different dielectric properties[KW16].

3.2.1 Physical Principle

Moving electric charges cause electric and magnetic fields, described by the *Liénard–Wiechert potentials*. When these fields change, energy in the form of electromagnetic radiation must be emitted. Causal for the emission of Transition Radiation (TR) is formally the change in the refractive index $n = \sqrt{\epsilon\mu}$ of the surrounding medium [Gre00]. This alteration in the dielectric properties around the charged particle, also changes its phase velocity $c_{\text{ph}} = \frac{E}{p} = \frac{\omega}{k}$ (with $k \sim n$) [KW16]. Formally the field of a particle entering a medium with a different refractive index changes to ensure continuity of the electromagnetic field conditions at the interface. This requirement is dictated by Maxwell's equations, derived from a shrinking Gaussian box on a Stokes surface.

3.2.2 Radiation Characteristics

For a relativistic particle with a Lorentz factor $\gamma \gg 1$ a energy spectrum for the TR can be derived, as given detailed in [AW12] and [KW16]. The radiation characteristic per radiation angle θ following, is cylindrical symmetric. So the radiation pattern is cone shaped, with a most probable radiation angle $\theta_{\text{max}} \approx {}^{1}/_{\gamma}$ [Gru93]. For ultra relativistic particles, having a large Lorentz factor, the radiation therefore is strongly directed forward and thus almost parallel to the particle track. This makes it easy to match the detected Transition Radiation to a detected particle. Furthermore the entire radiated energy is rising linear with the Lorentz factor of the relativistic particle $\gamma = {}^{E}/_{m}$ [KW16].
This is an advantage over many other physical effects, like ionization or Cherenkov radiation, which are rising with the speed of a particle and therefore offer only limited identification possibilities for highly relativistic particles [Gru93]. While their speed is close to the speed of light and hardly changes, the Lorentz factor continues to increase with higher energies.
However, the mean emitted photon number, is in the order of magnitude of the fine structure constant $\alpha = {}^{1}/_{137}$ and therefore very low [Gre00].
The transition of a $5\,\text{GeV}$ electron ($\gamma \approx 10^4$) on a polyethylene foil for example

leads to a mean photon number of $\langle N \rangle = 0.05$ [KW16]. To increase this number multiple transitions whose radiations constructively interfere are necessary.

Multiple Interfaces In principle more transitions along a particle track lead to more Transition Radiation. Instead of achieving the multiple transitions with a stack of thin foils often foam or fiber materials are used that meet the requirements for the sequence of interfaces within the average. For the CBM TRD, the use of polyethylene foam films, having lots of interfaces due to the air filled PE bubbles, proved to be the best option [TDR18].

3.2.3 Detector Implementation

The photons from the radiator can, after their creation due to the transition of a charged particle, be detected. Gas-filled detectors filled with high atomic number gases such as xenon or krypton are suitable for this purpose, as they offer a high detection probability for Transition Radiation photons in the X-ray domain. Due to the small angle of the Transition Radiation ($\theta_{\max} \approx 1/\gamma$) a spatial separation between the particle track and the transition radiation photons can not be achieved and it is only detected as an additional charge deposition [KW16].
However this combined detection of particle track and transition radiation can be used for electron identification by momentum determination. Especially electrons and negative pions with the same energies are hard to distinguish in other detectors because of their same charge. However because the electrons[2] are much lighter than the pions[3], they have a vastly different Lorentz factor at the same energy. For instance, at $5\,\mathrm{GeV}$, pions with $\gamma(\pi^-) \approx 37$ generate almost negligible Transition Radiation, whereas electrons with $\gamma(e^-) \approx 10^4$ produce substantial amounts of it.
To detect as much TR from electrons as possible, it is best to split the effective length radiator into several readout units in layers.
The TR detector in the CBM experiment consisits four layers of detectors with several modules of a radiator and a read-out chamber each. Thus, an electron efficiency of 90% with a pion suppression factor of 20 is envisaged [TDR18].

[2] Electron mass: $m_{e^-} = 0.511\,\mathrm{MeV/c^2}$ [Tho13, p. 3]
[3] Pion mass: $m_{\pi^-} = 139.6\,\mathrm{MeV/c^2}$ [Tho13, p. 56]

3.3 Transition Radiation Detection at CBM

The Transition Radiation detector in the CBM experiment consists of two main parts. First it is composed of a $30\,\mathrm{cm}$ thick Radiator made from polyethylene foam films. Second it features the Read-Out Chamber as a Multi-Wire Proportional Chamber with an additional drift region. A schematic illustration of this setup is shown in figure 3.2.

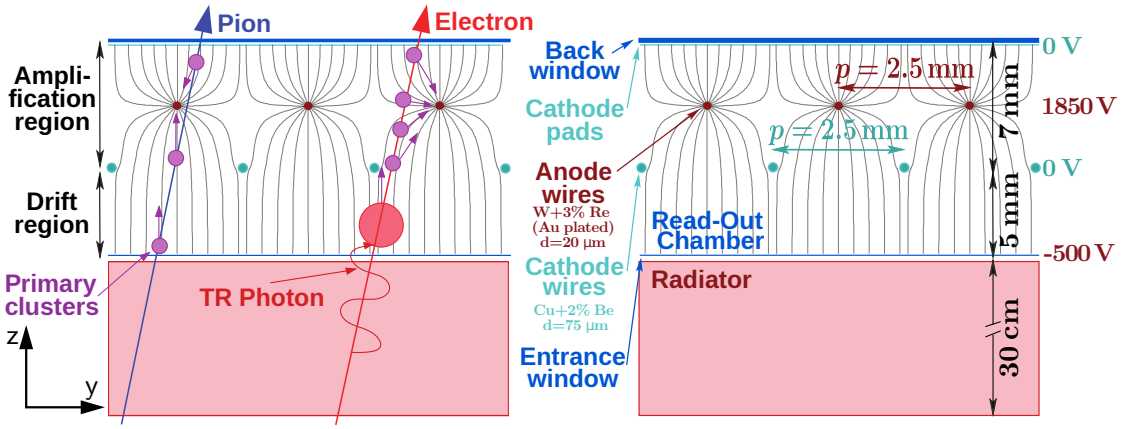

Figure 3.2: Schematic of depiction the CBM TRD. On the left, functional principle for the passage of a pion and an electron with generated TR. On the right, labeling of the individual parts, their dimensions and applied voltages [TDR18]. Modified from original.

The gas mixture in the ROC consists of 85% xenon because it has as other noble gases a high gas gain at comparative low voltages and a high absorption cross section in the X-ray domain for the TR photons. As a quencher gas 15% carbon-dioxide is added. This mixture leads to an absorption of the TR photons in the drift region directly behind the entrance window.

The input window consists of a $25\,\mu\mathrm{m}$ thin Kapton foil plated with aluminum, which is stabilized by a carbon lattice support grid. A drift voltage of $-500\,\mathrm{V}$ is applied to it, making the input window the cathode of the $5\,\mathrm{mm}$ long drift zone.

The integration of the drift zone within the ROC serves to increase the thickness of the gas volume, thereby enhancing the probability of TR photon absorption.

Unlike an expansion of the amplification region (anode-cathode spacing), this addition does not result in larger charge clusters induced on the cathode pads. The size of these clusters, as determined by the Pad Response Function and contingent upon the anode-cathode distance [Mat88], holds significance within the high occupancy region of CBM [TDR18].

Despite the drift, a time resolution between particles and TR photons cannot be achieved. Rather the presence of TR is only detected by the excess of the collected charge.

The entrance window envelops the gas volume towards the detector front, while the cathode pad plane encloses the detector towards the back. In figure 3.3, a cross-section of one ROC module illustrates this configuration.

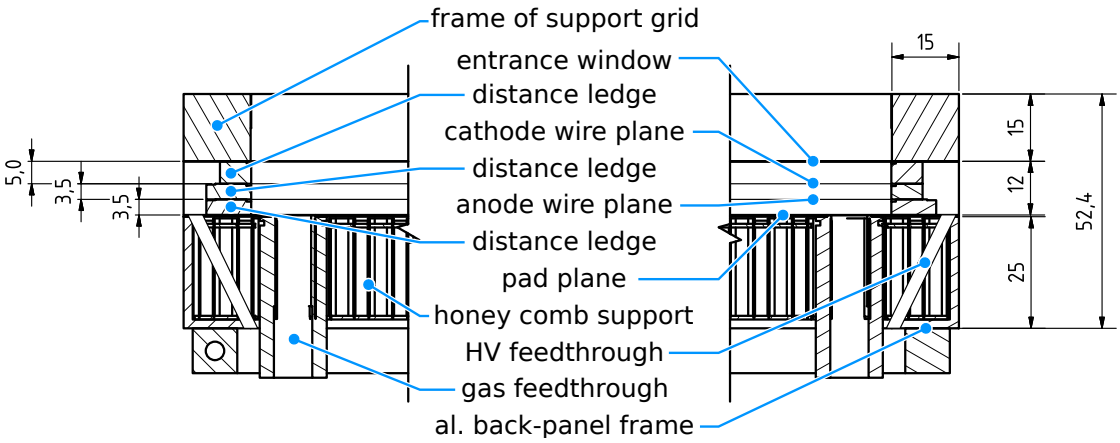

Figure 3.3: Horizontal cross section of a ROC module with dimensions given in millimeters [TDR18].

To the sides the detector volume is enclosed by the frames the wire planes are coiled and the distance ledges for the spacing. Simulations have shown that the best arrangement of the wires in terms of the electric field is a staggered arrangement with a distance of $2.5\,\mathrm{mm}$ between two identical wires and $3.5\,\mathrm{mm}$ of space between the anode and cathode wire planes, which adds up to an amplification region of $7\,\mathrm{mm}$ as shown in figure 3.2.

In addition, the wires are offset by $1.25\,\mathrm{mm}$ to the other wire plane, thus one wire is always exactly in the middle of two of the other wires. The voltage of the amplification region applied between the anode and cathode is $1850\,\mathrm{V}$.

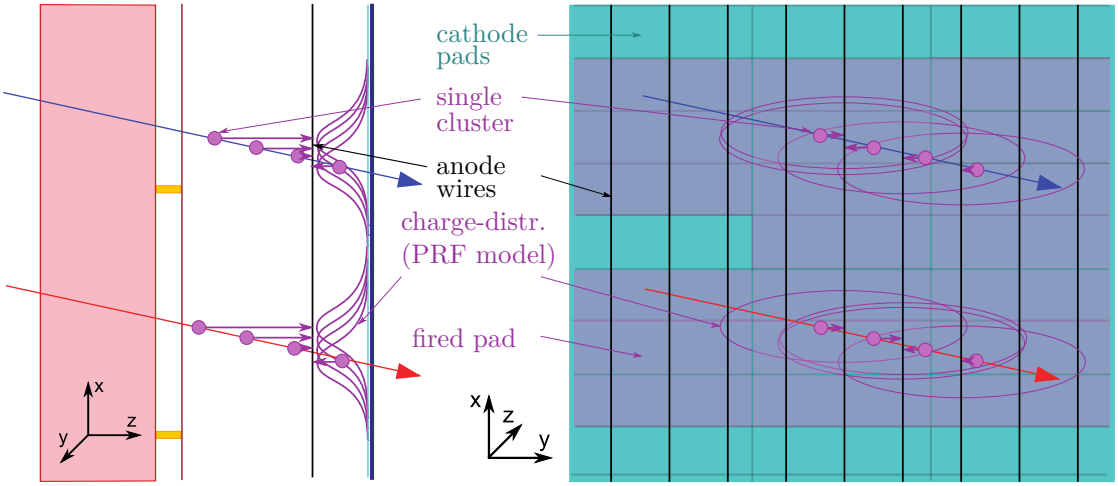

Figure 3.4: Schematic view of the distribution of the charges, generated by a particle going through the detector, on a section of the pad plane. [TDR18].

As previously explained only the induced charges at the cathode pads are used as the signal. The pad plane layout incorporates rectangular pads, whose widths along a pad row, are dictated by the distance between the pad plane and the anode wire grid. In addition to the heights of the pads along a column these values are optimized to ensure an optimal charge distribution among adjacent pads (10%/80%/10%), thereby achieving superior energy and position resolution. The pads are oriented as shown in figure 3.4 with there width in the direction along the wires and their heights, which are always a multiple of the anode wire pitch of $2.5\,\mathrm{mm}$, in the direction rectangular to the wires. According the Pad Response Function the high resolution of $200\,\mu\mathrm{m}$ to $300\,\mu\mathrm{m}$ is only achieved along the columns of the pads. In order to achieve a high spatial resolution in both directions the TRD layers are rotated by $90°$ each.

Composition of the TRD Station

As indicated above, one TRD layer consists of several modules. Because the hit rate gets higher the closer to the center, the modules and pad sizes are scaled in order to achieve uniform low detector occupancies and hit rates per read out pad. A total of four different module types are planned, which are arranged as shown in figure 3.5.

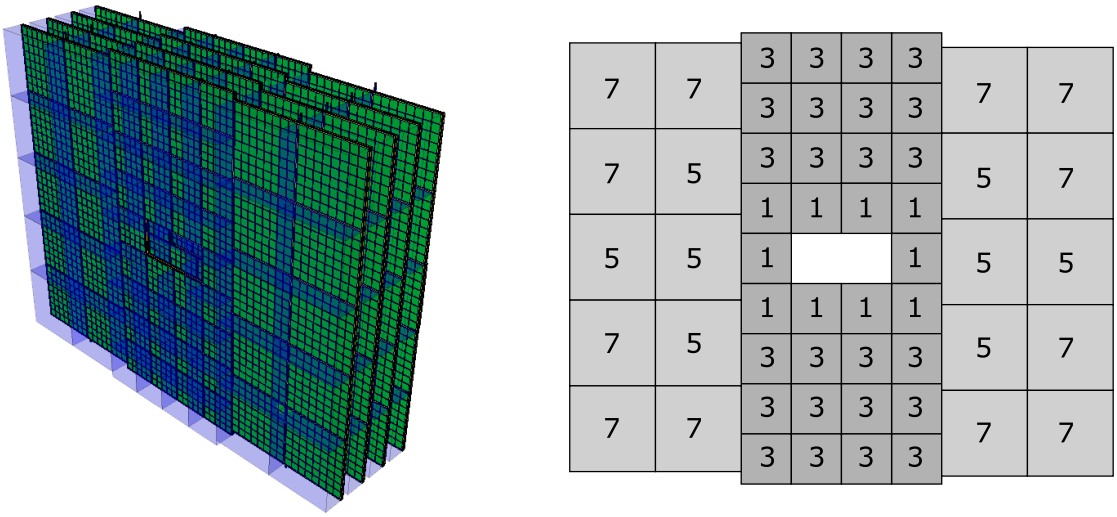

Figure 3.5: Left: The CBM TRD station with four layers of detectors shown from the front. Right: The arrangement of the different module types in one layer [TDR18].

Each module has a different pad size, but there are only two different outer dimensions of the modules. The different module types and pad sizes can be found in table 3.1.

Table 3.1: Summary of the dimensions and quantity of the different TRD detector modules and cathode pads within them [TDR18].

Module type	**1**	**3**	**5**	**7**
Number per layer	10	24	8	12
Outer Dimension	$57\,\mathrm{cm} \times 57\,\mathrm{cm}$		$99\,\mathrm{cm} \times 99\,\mathrm{cm}$	
Active area	$540\,\mathrm{mm} \times 540\,\mathrm{mm}$		$960\,\mathrm{mm} \times 960\,\mathrm{mm}$	
Average wire number per plane	216		384	
Pad size height x width both in mm	17.5×6.8	67.5×6.8	40×6.7	120×6.7
Pad number colums x rows	80×32	80×8	144×24	144×8

Furthermore, it has been proposed splitting up the pads of the innermost module type into two rectangles in order to achieve a uniform spatial resolution in two dimensions [Apr23].
With the different pad and module sizes, this results in a total number of 54 modules per layer with $82\,432$ pads read out per layer. Thus the entire TRD station consisting of four layers, requires the production of a total of 216 modules and almost $33\,000$ readable channels.

The preceding discussion highlights the various factors that are important in regard to the TRD station in the CBM experiment and shows the range of considerations that are crucial for its optimal functioning. The following section focuses on one specific aspect - the wire tension - and describes different ways in which this can be ensured in production.

4 Wire Tension

4.1 Electric Field

The electric field in the Read-Out Chambers (ROCs) crucially depends on the quality and the position of the anode and cathode wires. The wires can be approximated by infinitely extended line charges. The potential of the electrode arrangement as shown in figure 3.2 can only be determined numerically. The anode wires are approximated as an infinite number of line charges, extended also infinitely in x-direction. The y distance $p = \Delta y$ is set to the known wire pitch. With the load per length on the line charges $\lambda = {}^{\mathrm{d}q}/_{\mathrm{d}x}$ and the electrical field constant ϵ_0 the potential follows as [MF53]:

$$\phi_0(y,z) = -\frac{\lambda}{2\pi\epsilon_0}\ln\left(2\sqrt{\sin^2\left(\frac{\pi y}{p}\right)+\sinh^2\left(\frac{\pi z}{p}\right)}\right) \tag{4.1}$$

At $z \gg 0$ this potential gets independent of y, like the one of a plate capacitor, forming equipotential planes [KW16]. This makes it possible to place the cathodes at $z = \pm h$ with $h \gg p$. This leads to an approximated total potential as:

$$\phi(y,z) = \phi_0(y,z) + \frac{\lambda}{2\epsilon_0}\frac{h}{p} = \frac{\lambda}{2\pi\epsilon_0}\left[\frac{\pi h}{p} - \ln\left(2\sqrt{\sin^2\left(\frac{\pi y}{p}\right)+\sinh^2\left(\frac{\pi z}{p}\right)}\right)\right]$$

On the other hand for small values of z and values of y in a periodicity of the pitch p ($n = 0, \pm 1, \ldots$) the potential is cylindrically symmetrical [KW16]:

$$\phi(y,z) \to \phi(r) = \frac{\lambda}{2\pi\epsilon_0}\left[\frac{\pi h}{p} - \ln\left(\frac{2\pi}{p}r\right)\right] \quad \text{with} \quad r = \sqrt{(y+n\cdot p)^2+z^2} \tag{4.2}$$

This means that the surface of the wires can be considered equipotential planes. With this approximation the anode wires can be assumed to have an radius R and λ can be interpreted as a surface charge per length.

This approximation is therefore sufficient in the boundary conditions of the arrangement in the ROCs. The electric field close to the wires is pointing in the direction of the radial unit vector $\vec{e}_r$ and can then be obtained as:

$$\vec{E}(r) = -\frac{\partial\phi(r)}{\partial r}\vec{e}_r = \frac{\lambda}{2\pi\epsilon_0}\frac{1}{r}\vec{e}_r \tag{4.3}$$

The $E \sim {}^1\!/_r$ dependency shows that the closer the field is to the wire, the larger it becomes. This also means, that the smaller the diameter of the wires, the greater the electric field strength gets in their immediate vicinity. In order to achieve a sufficient gas amplification, very thin anode wires are therefore preferred.

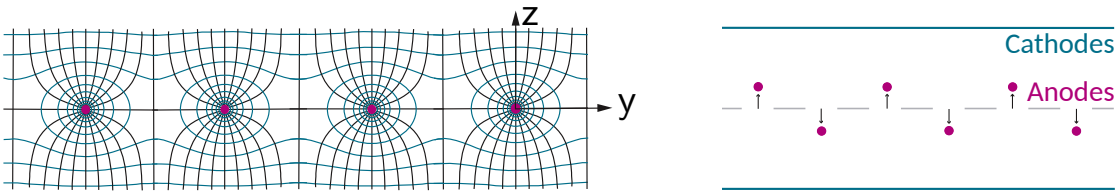

Figure 4.1: Left: Typical potential (blue) and field lines (black) in a MWPC [KW16]. This depiction shows that the potential becomes radially symmetrical near the wire and independent of y near the cathodes.
Right: Anode wires alternately displaced in opposite directions by the electrostatic forces [KW16].

4.2 Wire Sag

As identical charges repel each other according to Coulomb's law, a repulsive force also acts on the wires in a plane. If no force completely compensates this, the wires will displace with respect to their field-free positions. The electrostatically stable configuration is shown in figure 4.1 (right), where neighboring wires are alternately deflected in opposite directions [KW16].

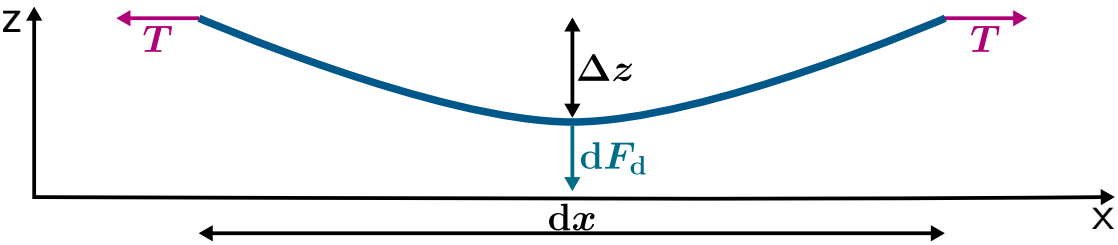

Figure 4.2: Schematical view of the wire sag caused by a force F_d acting on a wire stretched with the tension T.

The only remaining force that opposes the deflection is the restoring force resulting from the tension with at the wires are stretched. Naturally, a wire that is stretched on both sides will sag in the middle as shown in figure 4.2, depending

on how strong the force of this tension is. In a general case, the force $\mathrm{d}F_\mathrm{d}$ acts on the wire per unit length $\mathrm{d}x$, resulting in the simple relation:

$$\mathrm{d}F_\mathrm{d} = \kappa \mathrm{d}x \tag{4.4}$$

with a proportional constant κ. In the simplest case of the deflecting force is the weight force $\mathrm{d}F_\mathrm{d} = \mathrm{d}F_\mathrm{g}$ of a section with the mass $\mathrm{d}m$ and the length $\mathrm{d}x$, the connection is following [BR08]:

$$\mathrm{d}F_\mathrm{g} = \mathrm{d}m \cdot g = \rho \cdot \mathrm{d}V \cdot g = \rho \cdot A \cdot \mathrm{d}x \cdot g \quad \Rightarrow \quad \kappa = \rho \cdot g \cdot A \tag{4.5}$$

With the gravitational acceleration g and cross section A and the density ρ of the wire.

The deflecting force $\mathrm{d}F_\mathrm{d}$ must be compensated by the vertical component of the wire tension $\mathrm{d}F_\mathrm{t}$ as shown in figure 4.2 on every point x. This restoring force is equal to the horizontal pulling force or tension T, which stretches the wires to the chamber walls, multiplied with the difference of the slopes z' at the two ends of the interval $\mathrm{d}x$:

$$\mathrm{d}F_\mathrm{t} = -T \cdot [z'(x + \mathrm{d}x) - z'(x)] \tag{4.6}$$

The compensation $\mathrm{d}F_\mathrm{d} = \mathrm{d}F_\mathrm{t}$ now leads to:

$$\frac{\kappa}{T} = -\frac{z'(x + \mathrm{d}x) - z'(x)}{\mathrm{d}x}. \tag{4.7}$$

In the limit this results in the second derivative giving the differential equation:

$$z'' + \frac{\kappa}{T} = 0 \quad \text{with} \quad \frac{\kappa}{T} = C = \text{const.} \tag{4.8}$$

Two times integrating gives the solution:

$$z(x) = -\frac{C}{2}x^2 + ax + b. \tag{4.9}$$

With the boundary condition that there is no sag at the suspension points[1] the two constants a and b can be determined as:

$$a = 0 \qquad \text{and} \qquad b = \frac{C}{2}\frac{l^2}{4}.$$

This results in the following solution regarding the wire sag Δz:

$$\Delta z = z(x) = -\frac{C}{2}x^2 + \frac{C}{2}\frac{l^2}{4} = \frac{\kappa}{2T}\left(\frac{l^2}{4} - x^2\right). \tag{4.10}$$

At $x = 0$ the wire sag is at its maximum:

$$\Delta z_\mathrm{max} = z(0) = \frac{\kappa l^2}{8T} \quad \text{and for} \quad \mathrm{d}F_\mathrm{d} = \mathrm{d}F_\mathrm{g} \quad \Rightarrow \quad z(0) = \frac{\rho A g l^2}{8T}.$$

The $\Delta z \sim {}^1\!/_T$ dependency shows that the greater the mechanical tension on the wires is, the smaller is the wire sag.

[1] The wire with the length l is fixed at $x = \pm\frac{l}{2} \Rightarrow z\left(\pm\frac{l}{2}\right) = 0$

Regarding the anode and cathode wires in a big CBM TRD chamber the wire sag in the middle of the chamber according to this formula and with just the gravitational force acting on the wires would be:

$$\begin{aligned} \text{Anode}: &\quad \Delta z_{\max} = 13.63\,\mu\text{m} = 0.68 \cdot d_a \\ \text{Cathode}: &\quad \Delta z_{\max} = 41.24\,\mu\text{m} = 0.55 \cdot d_c \end{aligned}$$

The saggita are also represented as a multiple of the respective diameter d.

If the wire length and its material are specified, a sufficient wire tension is required to keep the sag sufficiently low. However, the tension cannot be increased arbitrarily for two reasons. First, the chamber must be able to withstand the sum of the tensions from all the wires. The less rigid the chamber frame is, the more it bends leading to shorter and less tense wires towards the center.
The second limiting factor is that above a maximum pulling force T_c inelastic deformations can occur as outlined in appendix B. The ratio T_c/A is constant and often called yield point R_e. Usually in order to keep the sag as minimal as possible, the force of tension is close to this limit [BR08], which is why materials with a high yield point must be chosen.

In total three forces act on each wire resulting in a differential equation of the form [Gru93]:

$$T \cdot z''(x) + f_e(z) + \rho A g = 0 \tag{4.11}$$

The contributions of the restoring force resulting from the wire tension and the gravitational force are known from the previous consideration. Here additionally the electrostatic force $f_e(z)$ has to be considered.
The gravitational and electric field component do not have to point in the same direction. Depending on the orientation of the wires, the gravitational component can strengthen or weaken the electrostatic contribution. In the CBM experiment the modules are rotated by $90°$ with each layer, in order to achieve a high spatial resolution in x- and y-direction. The wires of every second level therefore run vertically, which means that gravity acts in the direction of the wires and therefore makes no contribution to the sag.
The precise considerations of the electrostatic force, as outlined [Mah04] and [BR08], must take into account various dependencies.

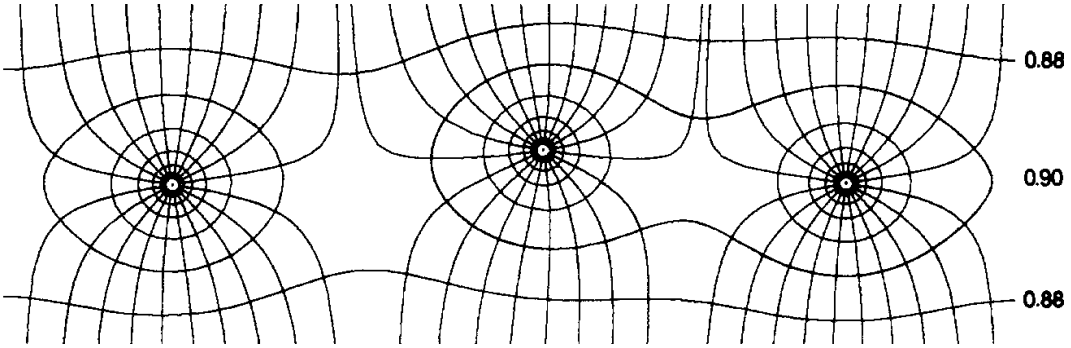

Figure 4.3: Electric field lines and potential lines with proportion of total potential around the anodes. One wire is displaced by 10 percent in the y- and z-directions with respect to the original wire spacing [Ers72].

A displacement of the wire position changes the shape of the electric field as shown in figure 4.3 and therefore alters the amplification process, leading to variations in amplification among different wires.

In appendix A some simulations from [Mah04] used for these considerations regarding the TRD modules of the ALICE experiment can be found.

For the CBM TRD modules, evaluations of the detection with the mechanical and material aspects led to the following choice of wire dimensions and material.

Table 4.1: Summary of the wire data used to calculate the wire sag and the oscillation frequency. Nominal values as outlined in [TDR18] are used (see appendix B).

	Density ρ in $\mathrm{g/cm^3}$	Diameter d in µm	Cross section A in $\mathrm{mm^2}$	Length l in mm	Tension T in N
Anodes	19.3	20	$3.142 \cdot 10^{-4}$	960 or 540	0.5
Cathodes	8.15	75	$4.418 \cdot 10^{-3}$	960 or 540	1

4.3 Wire Selection

The values for the different quantities characterizing the wires can be found with their detailed sources in appendix B. All the relevant values are summarized in table 4.1.

Anodes In regard to the anode wires, the focus is on the wires having a small diameter in order to generate a high field strength in their vicinity. The exact wire diameter results from the tuning of the PFR to achieve the desired charge distribution on the pads is $d_a = 20\,\mu\mathrm{m}$. In order to stretch a wire with such a small diameter a very strong material has to be chosen. The material that has been chosen is a tungsten rhenium alloy W + 3%Re that also provides a good conductivity and has a very high yield point of $R_e = 1639\,\mathrm{N/mm^2}$. In order to have a smooth surface generating a uniform electric field the anode wires are additionally coated

with gold. The tension is chosen to be $T_a = 0.5\,\mathrm{N}$ resulting in a mechanic stress of $\sigma \approx 1575\,\mathrm{N/mm^2}$ very close to the yield point.

Cathodes The cathode wires do not have to have a small diameter. On the contrary, a small diameter would even be unfavorable because at their location the field should be as planar as possible. And wires with larger diameters can also better balance the electrostatic force between the anodes and the cathode pads in the back [Mah04]. The preferred diameter for the cathodes is $d_a = 75\,\mu\mathrm{m}$. But since larger wires also imply a larger gravitational sag, the cathode wires should be made out of a light material. An copper alloy with 2% beryllium does provide this, but has to be stretched with a larger force of $T_c = 1\,\mathrm{N}$ due to its greater weight.

Wire Length By default, the ledges to which the wires are attached as well as the frame of the support grid are $15\,\mathrm{mm}$ wide. The length of the wires is therefore exactly twice this width shorter than the outer dimensions (see table 4.1). However, the width of the ledges may also be reduced to $12.5\,\mathrm{mm}$ for the smaller chambers (type 1&3) in order to enlarge the active area.

4.4 Determination of the Wire Tension

To measure the tension of the wires multiple approaches are possible. The problem of measuring the tension mechanically by stretching the wires perpendicular to their direction is that they are really sensitive to breakage or inelastic deformation. Furthermore a physical contact to the wires could damage their surface.
Preferably the determination of the wire tension can be done automatically and touchless. Therefore the wire must be detected first, which has the advantage that the exact positioning of the wires can also checked at the same time. A promising approach for this is to use the natural oscillation of the wires, because this depends on their tension, as will be derived below. First the speed of a transverse wave travelling through a plucked wire is deducted following [LSM16].

As before a small length element $\mathrm{d}x$ of the wire is to be considered. For a wire with a constant density ρ a mass per length l can be defined as:

$$\mu = \frac{m}{l} = \frac{\rho \cdot V}{l} = \rho \cdot A. \tag{4.12}$$

The length element $\mathrm{d}x$ thus has a mass of $\mathrm{d}m = \mu \cdot \mathrm{d}x$. For a taut wire at rest (equilibrium) the tension on both sides of a length element must be equal. If this

taut wire is now plucked perpendicular, the mass element oscillates in this direction because of a restoring force resulting from the tension, and a transverse wave moves in the direction of the wire.

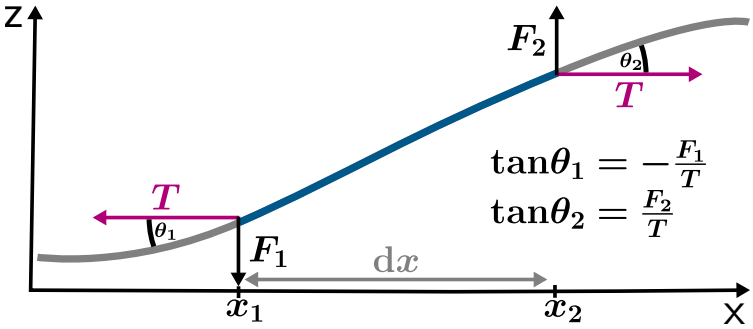

Figure 4.4: Schematically view of a wire element while a transverse wave is travelling along it.

If the deflection is small, the tension can be still only be considered to act horizontally and the horizontal distance between the points x_1 and x_2 is still $\mathrm{d}x$. Such a deflected length element is schematically shown in figure 4.4. With the small angle approximation the tangent of the angle between the two forces acting on the points x_1 and x_2 becomes the slope there:

$$\left(\frac{\partial z}{\partial x}\right)_{x_1} = -\frac{F_1}{T} \qquad \text{and} \qquad \left(\frac{\partial z}{\partial x}\right)_{x_2} = \frac{F_2}{T}. \tag{4.13}$$

The x-components of the force cancel each other and therefore the net force on the wire element equals the sum of the y-components:

$$F_{\text{net}} = F_1 + F_2 = T\left[\left(\frac{\partial z}{\partial x}\right)_{x_2} - \left(\frac{\partial z}{\partial x}\right)_{x_1}\right]. \tag{4.14}$$

According to newtons second law this is equal to:

$$F_{\text{net}} = \mathrm{d}m \cdot a = \mu \cdot \mathrm{d}x \cdot \frac{\partial^2 z}{\partial t^2} \tag{4.15}$$

$$\Rightarrow \quad \frac{\left(\frac{\partial z}{\partial x}\right)_{x_2} - \left(\frac{\partial z}{\partial x}\right)_{x_1}}{\mathrm{d}x} = \frac{\mu}{T}\frac{\partial^2 z}{\partial t^2} \quad \text{and in the limit:} \quad \frac{\partial^2 z}{\partial x^2} = \frac{\mu}{T}\frac{\partial^2 z}{\partial t^2}. \tag{4.16}$$

Compared to the linear wave equation in one dimension [LSM16]:

$$\frac{\partial^2 u(x,t)}{\partial x^2} = \frac{1}{v^2}\frac{\partial^2 u(x,t)}{\partial t^2}. \tag{4.17}$$

the speed of the wave on the stretched wire can be determined as:

$$v = \sqrt{\frac{T}{\mu}} = \sqrt{\frac{T}{\rho \cdot A}} = \sqrt{\frac{4T}{\pi \rho d^2}}. \tag{4.18}$$

In order to not have the wave cancel itself through interference, the length l of the wire must be a multiple of half the wavelength λ [LSM16]:

$$l = n \cdot \frac{\lambda}{2} \quad \Rightarrow \quad \frac{v}{f} = \frac{2l}{n} \qquad \text{with} \qquad n = 0, 1, 2, \ldots . \tag{4.19}$$

Here the definition of the wavelength $\lambda = {}^{v}/_{f}$ was applied. With the speed from equation (4.18) the fundamental frequency ($n = 1$) of the vibrating wire follows as:

$$f_0 = \frac{1}{d \cdot l}\sqrt{\frac{T}{\pi\rho}}. \tag{4.20}$$

On the other hand the wire tension can be calculated from this frequency with:

$$T = \pi\rho f_0^2 l^2 d^2. \tag{4.21}$$

With just the known wire properties length l, density ρ and diameter d and the fundamental frequency f_0 the tension can be determined. The expected frequencies for the correct wire tensions are listed in table 4.2.

Table 4.2: Expected frequency of the fundamental oscillation depending on the respective wire length and tension. With the data of table 4.1 in equation (4.20).

Module type	1 & 3	5 & 7
f_{anode}	266 Hz	150 Hz
f_{cathode}	154 Hz	87 Hz

4.4.1 Frequency Analysis

To determine the fundamental frequency of the oscillating wire from the periodic voltage signal, data fitting methods may lack frequency resolution and noise reduction, while still requiring many computational resources. In contrast, an analysis of the frequency components in the signal offers efficient noise without the need for a specific model. Mathematically, this can be achieved by calculating the frequency spectrum using a Fourier transformation. As the signal is not continuous but consists of discrete data points, a Fast Fourier Transform (FFT) is performed.

The FFT algorithm is based on the Discrete Fourier Transform (DFT), which decomposes a sequence of complex numbers into a series of sinusoidal components with different frequencies. Given a sequence $x_0, x_1, x_2, \ldots, x_{N-1}$, the DFT X_k is computed as:

$$X_k = \sum_{n=0}^{N-1} x_n \mathrm{e}^{-i2\pi kn/N}, \tag{4.22}$$

with i the imaginary unit and N the number of samples in the time-domain signal [Pre07]. The frequency index k ranges from 0 to $N-1$ and each value of k corresponds to a specific frequency component f_k in the frequency domain.

Equation (4.22) requires N^2 multiplications, but via the FFT algorithm this can be

reduced to a process of $O(N \log_2 N)$, making it suitable for real-time signal processing tasks [Pre07].
The maximum frequency that can be accurately represented in a digital signal, is the Nyquist frequency, given as half the sampling frequency: $f_{\text{Nyquist}} = {}^{f_s}/_2$, where $f_s = {}^1/_{\Delta t}$ is connected directly to the difference between consecutive samples Δt. The *sampling theorem* states, that only signals bandwith limited below f_{Nyquist} can be completely reconstructed by their samples [Pre07].
The FFT spectrum ranges from $-f_{\text{Nyquist}}$ to f_{Nyquist} and is symmetric for real valued signals as in this case. The presence of negative frequencies in the spectrum arises due to the nature of the Discrete Fourier Transform[2]. Because the number of the samples in the time domain and the number of frequency components are both equal to N, the frequency resolution Δf_{FFT} follows as [Pre07]:

$$\Delta f_{\text{FFT}} = \frac{f_s}{N} = \frac{1}{N \cdot \Delta t} = \frac{1}{t_{\text{ges}}}, \tag{4.23}$$

with t_{ges} the total duration of the measurement. Therefore in a ten second scan of the oscillating wire a frequency analysis with a resolution of $\Delta f_{\text{FFT}} = 0.1\,\text{Hz}$ can be achieved.
Furthermore, it is important to note that frequency components in the signal that exceed the Nyquist frequency are not determined correctly. Those higher frequency components "fold back" into the lower frequency range during the FFT computation. This effect is known as aliasing because the component appears at a wrong frequency within the Nyquist frequency range. Due to the periodicity, the aliased signal components appear at several points in the spectrum. The first alias is at [Pre07]:

$$f_{\text{aliased}} = \pm(f_{\text{Nyquist}} - |f_{\text{original}} - \cdot f_{\text{Nyquist}}|). \tag{4.24}$$

These peaks furthermore do appear periodically with a distance of f_{Nyquist}.
To reduce aliasing the sampling frequency should be chosen high enough or the data have to be lowpass filtered before the FFT is calculated. To determine the wire tension, first the FFT is calculated with scipy.fft and then the fundamental frequency is picked as the lowest frequency with a peak in the spectrum besides the DC component with scipy.signal.find_peaks.

[2] Positive frequencies representing components that oscillate in the forward direction of time and negative frequencies representing components that oscillate in the reverse direction of time for complex signals. For $k = 0$, $f_k = 0$ represents the DC component or the average value of the signal. For $k = 1$ to $k = {}^N/_2$ the positive frequencies ($f = 0 \ldots f_{\text{Nyquist}}$) and from $k = {}^N/_2 + 1$ to $k = N - 1$ the opposing negative frequencies are calculated.

5 Experimental Setup

The production process of the CBM TRD Read-Out Chambers will be done in an ISO-7 cleanroom, where one type of wire will initially be wound onto a transfer frame. This is done with a special machine that is designed to keep the wire tension as constant as possible. The winding frame must also meet special requirements in terms of rigidity. The winding creates two planes of wires, one on each side of the frame. First, both wire layers are glued on both sides and then the frame is divided into the two halves (wire levels) [TDR18]. In this way, two layers of one type of wire (for two chambers) are wound at the same time. Once a chamber has been built up to the ledges on which the anode wires rest, the (half) transfer frame with one anode plane is placed on top. No additional force should be exerted on the wires so that their tension does not change. Once the anode wires have been glued and soldered, they are cut off the transfer frame and another distance ledge and the cathode wire plane follows in the same way.

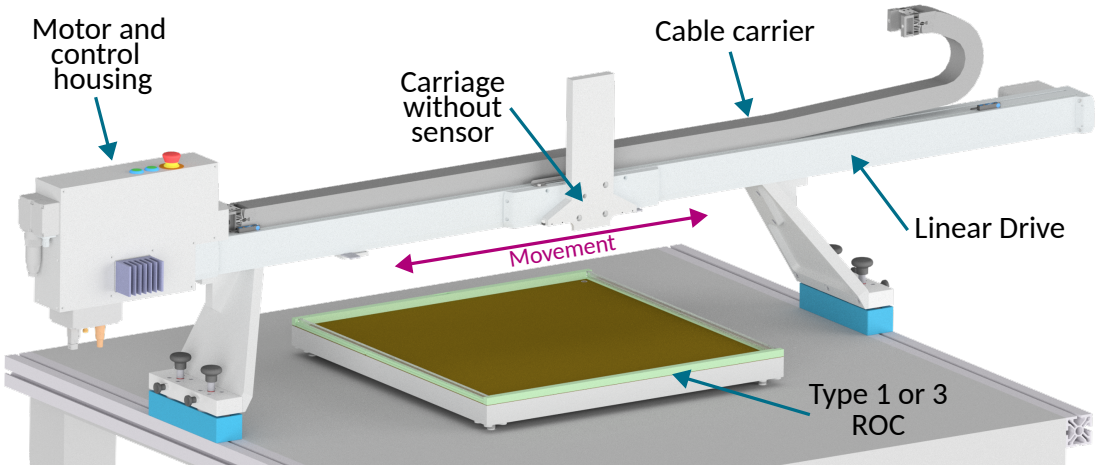

Figure 5.1: Schematical view of the WTTD on top of a chamber.

Between the mounting of the two planes, the tension of the anode wires has to be measured. Therefore, the Wire Tension Testing Device (WTTD) is placed in the center on top of the chamber as shown in figure 5.1 and the sensor is moved crosswise to the wires. However, prior to this, the tension should be checked additionally on the transfer frame. In this way, the wire tension for the anode and cathode should be measured each once before and after they are attached to the chamber.

5.1 Working Principle

The optical sensor, equipped for both light transmission and reception, detects reflections from surfaces and converts them into electrical signals. These analogue voltage signals convey information about the reflection intensity within the focal plane of the sensor.

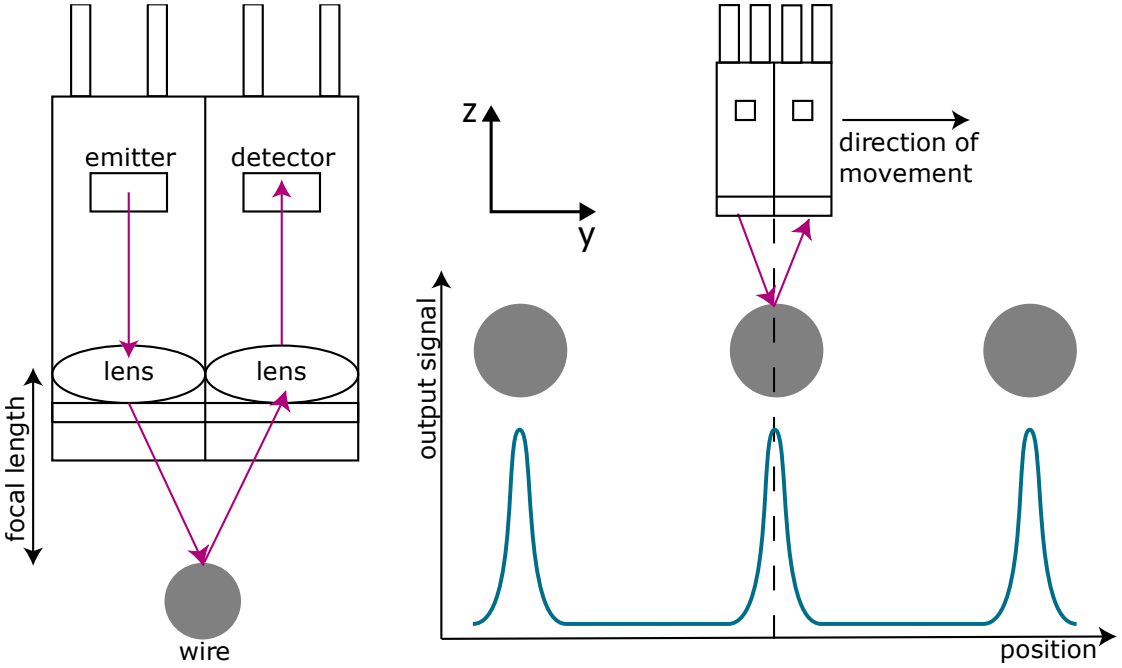

Figure 5.2: Schematic view of the sensor principle [Got05]. Modified from original.

The measurement method operates by placing the focal point of the sensor exactly in the wire plane, as depicted in figure 5.2 and then moving the sensor just perpendicular to the wire direction across the chamber.

Wire position When the sensor moves across the wires they move in and out of the focal point leading to a peak in the voltage output signal as shown in figure 5.2. The determination of the wire position is done by connecting the exact position information with these peaks.

Wire tension In a second run, the sensor is successively positioned at the detected wire positions. At each location, the wire is deflected by an air blast from a valve mounted next to the sensor. As the wire now oscillates in and out of the focus point, the voltage at the sensor output changes periodically with the given oscillation frequency of the wire. By reading out the signal and determining the fundamental frequency according to section 4.4.1, the wire tension can be calculated using equation (4.21).

5.2 Components

In order to measure the tension, various components are required, not all of which are shown in figure 5.1:

- **Mounting and stabilization** The device is positioned precisely, exactly parallel, reproducibly and secured against movement above the chamber or transfer frame using aluminium mounts.
- **Linear drive** The horizontal positioning of the measuring unit above the chamber is achieved with a linear drive. This uses the rotation of a threaded spindle under a cover strip to move the carriage, making it suitable for cleanrooms. The actual measuring unit is positioned horizontally above the wire level with a hand-operated fine drive on the traversing carriage.
- **Motor** To move the linear drive, a rotating DC motor with the corresponding control electronics is used. It is connected to the threaded spindle of the linear drive via a gear and an elastomere coupling to correct misalignments of the axes.
- **Measurement unit** The optical sensor is attached to the carriage of the linear drive pointing downwards together with a sensor module which connects it to the communication network as an ADC (Analog Digital Converter).
- **Air valve** The wires are deflected by an air blast. For this purpose a compressed-air line with a solenoid valve is attached next to the sensor.
- **Wiring** The connection of the electronic components is realized via a Controlled Area Network (CAN). In particular, the simultaneous monitoring of the position of the measuring unit with the signal from the sensor is the main focus here.
- **Processing** The position and wire tension determination should be controlled by a stand-alone computer that commands the movement and processes the data from the sensor.
- **Manual control** Additionally, the quality of the wires and solder joints is checked. Therefore the measurement unit on the linear drive will be exchanged with an optical microscope and the drive is operated with a manual control panel.
- **Security** To prevent accidents, the setup is equipped with an emergency stop switch and limit switches. Two of these are permanently attached to the ends of the linear drive and two remain movable in order to adapt them to the respective chamber size.

The entire WTTD is controlled by a Linux operated computer. It is connected to the network via a PC-CAN adapter (PEAK *PCAN-USB*) and acts as the master. As a particularity in the CAN network, every device is not directly connected to the master. Instead, there is one CAN line consisting of two twisted cables (CAN-High and CAN-Low) which are terminated at both ends with $120\,\Omega$ resistors. Each participant is connected to the main line via a junction (stub), which is why it is referred to as a node.

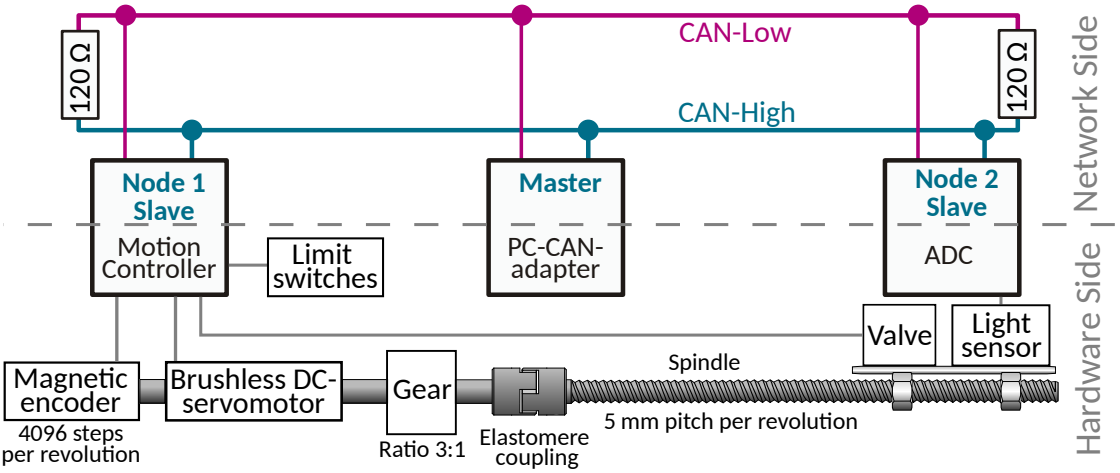

Figure 5.3: Schematic layout of the wire tension measurement setup.

In addition to the PC as the master, the two other participants on the network are the Motion Controller and the ADC. A schematic representation of the layout of all components is shown in figure 5.3.

While the ADC (MicroControl *sensor module µCAN.1.ai-SENSOR / voltage*) just digitalizes the voltage signal of the sensor (OMRON *EE-SPY402*), the Motion Controller has a wider functionality. This device (Faulhaber *MC 5005 S CO*) is the central control unit for the linear drive because it commands the movement of the motor and processes the position. Therefore, it is connected to the motor (Faulhaber *4490H048BS*) itself and the encoder. The latter (Faulhaber *AEMT-12/16 L*) breaks down each revolution of the motor into 4096 increments. Furthermore, the Motion Controller has analogue and digital inputs and outputs. These are used on the one hand for the limit switches, the control panel of the manual mode and the emergency stop and on the other hand to open and close the air valve.

Each revolution of the motor is converted via a gear into a third of a revolution of the threaded spindle. The linear drive (HIWIN *HM060S005*[1]) in which the spindle is mounted has a length of $130\,\mathrm{cm}$ and a feed constant of $5\,\mathrm{mm}$. To achieve a propulsion of $1\,\mathrm{cm}$, the motor must therefore perform six revolutions.

[1] The complete article number is `HM060S005C1300S000C2NN` which includes all specifications.

Not all of the final components are already present, as the setup is still under construction. However, all essential parts for the function are already present and connected via the CAN network.

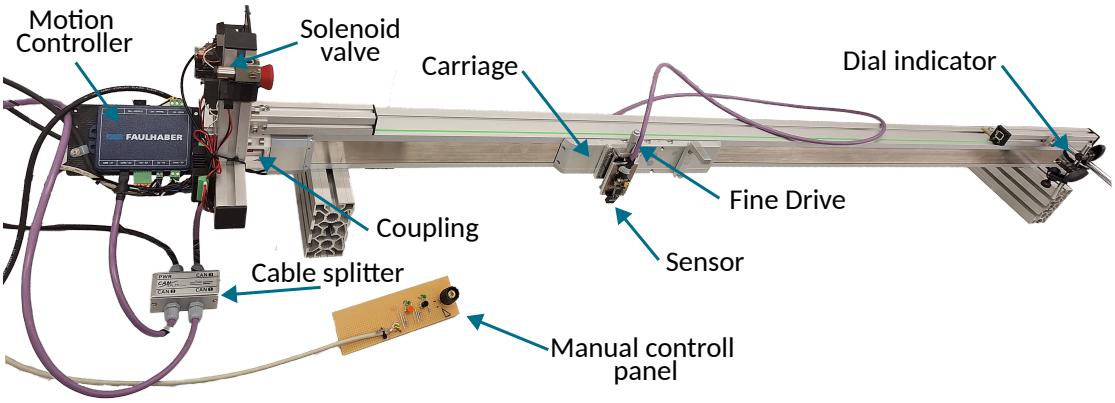

Figure 5.4: The current setup for wire tension measurement.

In the real setup shown in figure 5.4 the CAN line (purple) is terminated at the D-sub connector on the PC-CAN adapter and at the ADC because this is the largest distance in the physical network. The stubs going to these components before the resistors are therefore negligible. The line to the Motion Controller, on the other hand, branches off by about $20\,\mathrm{cm}$. This connection is made with the in-house manufactured *CAN-Split 3000 pro*, where a power line for the sensor is fed in as well. Conveniently, the CAN line used (LAPP *Unitronic Bus CAN*) has two pairs of cables, one of which is used for CAN-High and CAN-Low and the other for the power supply (V_{cc} & GND).

The ADC requires a supply voltage of $10\,\mathrm{V}$ and provides an output of $4.5\,\mathrm{V}$, which is sufficient to power the sensor. Furthermore, a voltage of $24\,\mathrm{V}$ must be provided for the Motion Controller, which also supplies the encoder, and an additional $48\,\mathrm{V}$ for the actual motor.

On the carriage of the linear drive, a table as shown in figure 5.5 is mounted which can be moved with the fine drive. Via this the focus point of the sensor can be exactly adjusted to the wire plane vertically.

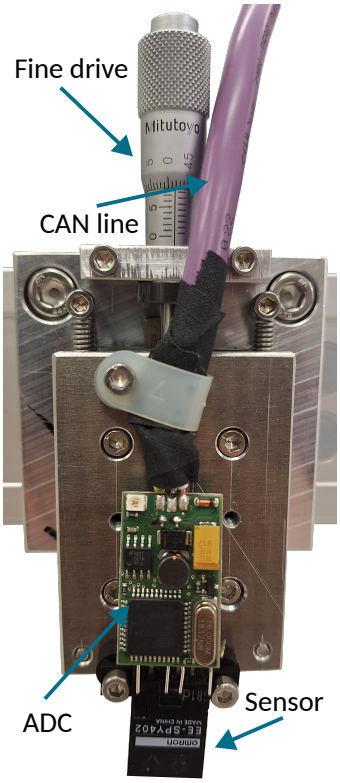

Figure 5.5: View of the measurement unit on the linear drive carriage.

5.3 CAN Network

To ensure the connection and the communication between the different electronic components in the WTTD a Controlled Area Network (CAN) is used. Precisely the protocol CANopen is implemented, which is based on CAN bus.

5.3.1 CAN Bus

CAN bus is a widely used serial field bus, which is resilient regarding electric disturbances and electromagnetic interference. While the term "field" denotes its application in controlling processes within a physical environment, "serial" refers to its primary characteristic: all network participants are connected serially through a shared transmission channel [PAK08]. Such a single communication way is simple and low cost compared to a complex direct wiring. Furthermore, it provides one point of entry to communicate with the whole network for diagnostics, data logging and configuration. A serial connection also ensures, that the data broadcasted on the bus reaches all other participants in the network. Each participant can then check the data and decide whether to receive and process or ignore it.

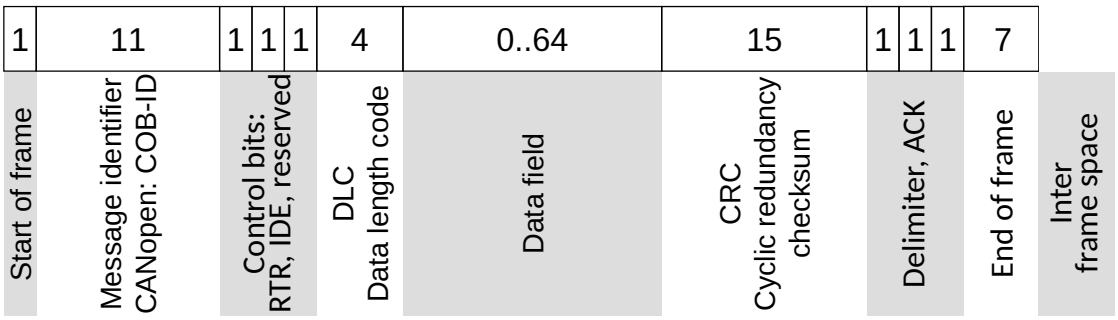

Figure 5.6: The structure of a CAN frame with its different sections and their length in bits (top) and their names (below) [PAK08].

Arbitration With CAN, each participant can start transmitting on its own. In order to ensure interference-free transmission despite this, all digital data frames have an address and are prioritized with a logical conjunction (AND). Each message has a message identifier for whose bits a 1 is always recessive and a 0 is dominant. This ID is 11 bit long, which means that $2^{11} = 2048$ different messages can be addressed.

While transmitting a message, the respective network participant is also monitoring the network to verify if the bits on the bus still match the one it has sent [Sch05]. If two participants start sending, the message with the higher priority prevails. This happens because if a participant sends a 1 but receives a zero, it withdraws from the bus and sends its information again later. In this way the data

with the highest priority gets immediate access to the bus without causing interruption with other frames. The disadvantage of this, is that all messages have to be sent sequentially. Furthermore, if data is transmitted between two participants, all others must remain silent.

CAN messages The complete structure of a CAN frame is displayed in figure 5.6. After the message identifier that is used for the data arbitration two control bits follow, for remote requests (RTR) and extended messages (IDE: identifier extension). After one reserved dominant bit the next four bits include the length of the data field in bytes $(0 \ldots 8)$. Up to this point, this was all the *frame header* and now does the data field begin. Here the data bytes are transferred in little endian byte order with the least significant byte first. After the data field the Cyclic Redundancy Checksum (CRC) and the acknowledgement bit (ACK), embedded in two recessive separator bits and set if the message has been read, follow. Each data frame then ends with 7 recessive bits and the next frame can only follow after at least 3 intermediate bits (inter frame space).

Various definitions are necessary to enable communication between devices via CAN. These include allocating CAN identifiers to individual devices, specifying transmitted data content, ensuring accurate interpretation of data, and implementing higher-level device monitoring. All of these functions are summarized in the application layer, for which the protocol CANopen is used in this case.

5.3.2 CANopen

In addition to CAN bus, which provides the transport layer the higher-layer protocol CANopen is used for the application. It is a communication protocol with standardized and manufacturer independent **device profiles** for many different appliances and in this case some for the general communication network (CiA 301, 302, 305), one for motion control (CiA 402) and one for the measuring unit (CiA 404).

Furthermore the CANopen standard, which is maintained by the organization CAN in Automation (CiA), provides **communication models** such as master-slave communication. For instance, the master sends a synchronization message and all respective slave devices record their measurement data at the time they receive this message.

This also has an impact on another important CANopen component, the **device states**, which describe the operational status of a device. This is because a master node can change the status of a slave node and thus activate and control it.

All parameters defining the behavior of a CANopen node are encapsulated within a standardized structure. All the data is read from or written to this **object dictionary** (OD), which can be understood as a data storage. The entries within the OD are addressed with a 16-bit index and sometimes additionally a 8-bit sub index. For example, the serial number of the device is deposited at the index `0x1018` and subindex `0x04` in the object dictionary of every node. The structure of the object dictionary is described in the **electronic datasheet** (EDS file), which acts as a library for the OD, with all its objects but not the values. These files are used by the program running on the PC that controls all the nodes to assign a command with the corresponding OD object.
To complete the six core concepts of CANopen [Fal22], which are highlighted in bold in the previous text, the last one, the **communication protocols**, is still missing. These define the actual communication between the participants and are described below.

5.3.2.1 Communication Protocols

CANopen encompasses a variety of communication services, including the NMT (network management) service, which regulates the state of network devices. Furthermore, communication services such as EMCY for error messages, HEARTBEAT for node monitoring and SYNC for synchronization are also incorporated. Among these, the protocols related to the recorded data are of particular importance and are described in more detail.

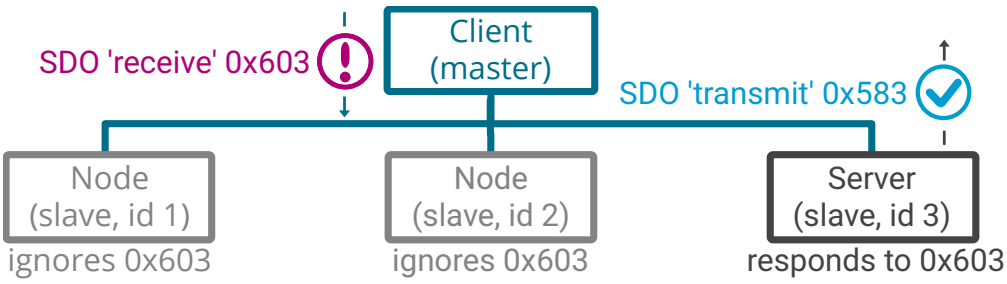

Figure 5.7: Visualization of the SDO communication [Fal22]. (Modified from original)

Service Data Objects The Service Data Object (SDO) service is used to access data in the object dictionary of a node from another node. An example is shown in figure 5.7, where a master node wants to request data from a special node. This uses the client-server communication model, where a client (the master) requests data from a server (slave). Thereby the terminology takes a server-side perspective, where the request is assumed as a received SDO message and the data sent is a transmitted SDO message.

The addressing is done by the message identifier which is called COB-ID (Connection Object ID) in CANopen. Its 11 bits are divided into a 4-bit function code and the 7-bit node number. A participant only responds if it has a matching node ID. The actual address of the data in the OD is then transferred via the data bytes of the can frame. In the reply message (transmit SDO), the requested data then follows behind.

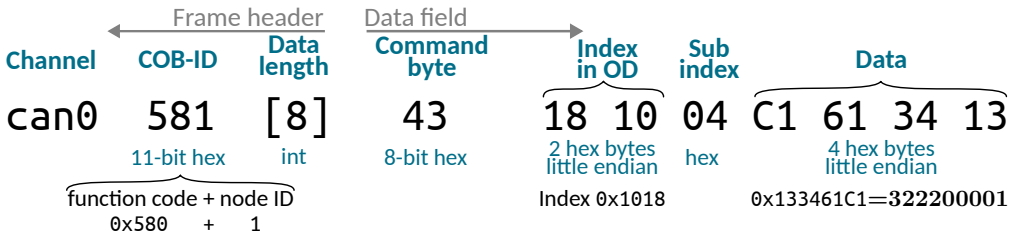

Figure 5.8: Structure of a SDO message as it is displayed with candump.

As two messages (request and response), called SDO channel, are always required for this type of transmission the communication is slowed down. Furthermore, the data that can be transmitted with the SDO service is restricted to 4 bytes, because the OD index and a command byte is transferred in the message. The SDO example in figure 5.8 shows how the transmit SDO containing the serial number (322200001 at OD index 0x1018–4) of node 1 is displayed in the candump view on the PC.
Due to their laboriousness, SDOs are only used in the control of the WTTD for configuration and for tasks where speed is not a priority, such as opening the solenoid valve.

Process Data Objects On the other hand all nodes can also send data independently without a request, if for example a measured value changes, a internal clock elapses or a sync message is received. This is achieved with the helf of the Process Data Object (PDO) service, which also does not have a long overhead and can thus carry the full eight bytes of data the CAN protocol does provide. To do this, one or more entries in the object dictionary are mapped to a PDO. Both the relevant node and the master must then know about this "mapping" in order to be able to assign the blank data to the correct entry.
Apart from the device states, it is primarily the position of the measuring unit and the measured value of the sensor that are transmitted via PDOs, as these are constantly changing and therefore cannot always be queried. This happens in interaction with the SYNC service, because each synchronization message triggers a measurement (as described above) and the transmission of the respective PDO. This makes it possible to identify the strength of the reflection at a specific position.

Control Software Implementation

6

This chapter examines the implementation and analysis of the Python-based control software used to control the operation of the measuring device.

```
from classes import Network, Motor, Sensor
Bitrate, sync_rate = 1e6, 400 #in bits/s, Hz

    # Connect to network and nodes by initializing the
       classes
network = Network(channel="can0", bitrate=Bitrate)
motor   = Motor(network ,r"EDS_motor.eds",1)
sensor  = Sensor(network,r"EDS_sensor.eds",2)

    # Enable the operation of the devices on the network
motor.turn_on(); sensor.turn_on()

    # Synchronize the Motion Controller and the ADC
network.sync.start(1/sync_rate)
# ---------------------------------------
# All measure functionality follows here
# ---------------------------------------
    # Stop the SYNC and finish the operation
network.sync.stop()
sensor.turn_off(); motor.turn_off()
network.disconnect()
```

Listing 6.1: General program code to operate the WTTD.

The general program code is outlined in listing 6.1. First, classes for the network, motor and sensor were defined. If these are called, the respective connection is also established with the initialization. To do this important parameters such as the SocketCAN channel, the bitrate, the EDS files and the nodenumbers are passed.

The two nodes can then be activated on the network. Once the nodes are in the

active network state, the actual sequence programs for the measurements can follow. Network synchronization is started for this purpose. Every $t_{\text{sync}} = 1/f_{\text{N}}$ interval, a sync message is sent to the network and the two nodes send their respective measurement data synchronized as PDOs. This makes it possible to simultaneously determine the position of the linear drive and the output signal of the sensor. It must be noted that the network syncing frequency f_{N} with which the data on the network is send, does not have to be the same frequency as the sampling frequency f_{s} of the sensor module. The lower one of these two frequencies is the decisive factor in the analysis of the frequency.
Once all control programs have been executed, the periodic transmission of SYNC impulses is stopped, the nodes are reset to a switched-off network state and the connection to the network is closed.
The classes of the individual instances are described in more detail in the following section.

6.1 Network

To set the network up several steps as displayed in figure 6.1 are needed. First it is checked whether there is a kernel module which serves as driver for the PEAK-System USB Interface. If no module is present, it is loaded into the linux-kernel using the `modprobe` command. Once this is done the CAN network should appear as a network interface whose properties are displayed via the `ip link show` shell command. If there is no output for this command, the CAN network is not physically connected. However, if there is an output it contains the status of the device and the current bit rate. If the network is already activated and the bit rate does not match the desired one, it must be changed. To avoid communication problems, the network connection is first disconnected and then restarted at the old bit rate. Using the Layer Settings Services (LSS), the nodes on the network are then set to *autobaud* mode, where they automatically recognize any bit rate and the network is restarted. Finally, using LSS, the desired bit rate is fixed again. In any case, the start-up and shutdown is achieved using the shell commands `ip link`

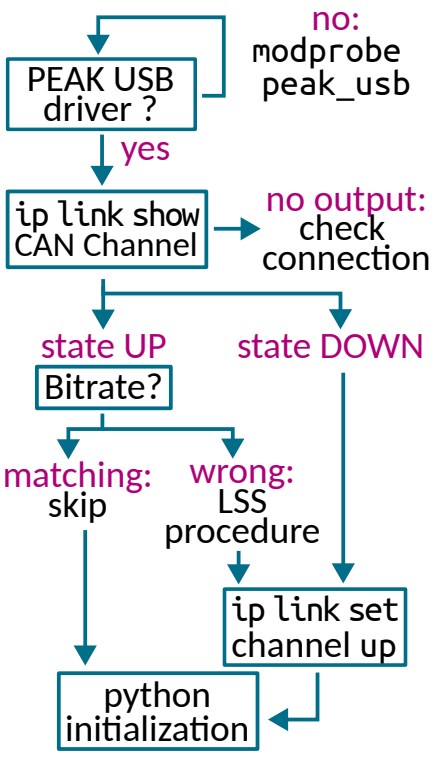

Figure 6.1: Block diagram of network initialization steps.

`set up` or `ip link set down`. Finally, the network is associated with the python `canopen` instances, thus shell commands are no longer required for any further initializations. The bit rate f_{Bit} is just the rate of the network and not equal to the syncing rate f_{N}, with which the measured values are retrieved or the sampling rate f_{s} of the sensor. During the following measurements the bit rate is set to the highest possible value that all nodes support: $f_{\mathrm{Bit}} = 1\,\mathrm{Mbit/s}$.

6.2 Motion Controller

The Faulhaber Motion Controller *MC 5005 S CO* controls the movement of the motor and therefore the linear drive. It also monitors the position using the data from the encoder. For this reason, the network node is sometimes simply referred as the motor or drive below. All parameters that describe the interaction of the individual parts, such as the length of the linear drive or the ratio of the gear, are permanently written as parameters of the object dictionary in the non-volatile memory of the motion controller. The motor position is therefore converted directly into the linear position of the carriage. Only the network and operation specific parameters have to be set before the Motion Controller is ready to be used.
To simplify these configurations, the device profile for drives and motion control (CiA402) is implemented with the python `canopen` environment. The profile provides power states that differ from the NMT network states and defines various operation modes. In this case, the profiled position mode (PP) is used, in which a target position is reached via a speed profile calculated by the Motion Controller. The actual operation is then based on two standardized message protocols for controlling (*Controlword*) and monitoring (*Statusword*) the motor node. These can be transmitted both as SDO and PDO and their individual bits enable the actual movement or indicate whether it has come to a (planned) stop.
Additionally Small BASIC programs are stored on the Motion Controller, which are used to control the linear drive in manual mode. These link the signals from the controller connected to the analog and digital inputs with the movement tasks.

6.2.1 Connection

As it is the case with the network, the connection to the Motion Controller is established during the initialization of its corresponding python class. After the node is introduced as a CiA402 instance in the `canopen` environment, a bootup message is triggered, using the Network Management (NMT) command `RESET COMMUNICATION`. Once the bootup message is received, the physical connection is ensured.After an error handler, which directly outputs emergency messages, has been linked, the

mapping of the PDOs is adjusted. The Process Data Object, which contains the position of the linear drive, is converted to synchronous transmission and other important parameters such as the profile speed and the operation modes are added to PDOs. Finally, the node is set up by exchanging some SDOs so that the power states defined in the CiA402 profile can be used.

6.2.2 Activation

Besides the NMT states that describe the state of a node regarding the network side the CiA402 profile defines power states in order to activate the motor for operation.
To switch the controller to the operational state, it is necessary to run through a standardized state machine. Depending on the initial state, different steps must be taken to enable the operation, which are implemented in the code. Regardless of which step is started, the power state must be set to `OPERATION ENABLED` to start the motor. At this point, the statusword is also monitored and if the motor cannot be started, for example because no voltage is applied to it, a runtime error is raised.

6.2.3 Operation

As described before, the drive to a target position is controlled by a speed profile running in the background once the movement is enabled. The start and the monitoring of this is done via a script which steps are depicted in figure 6.2.

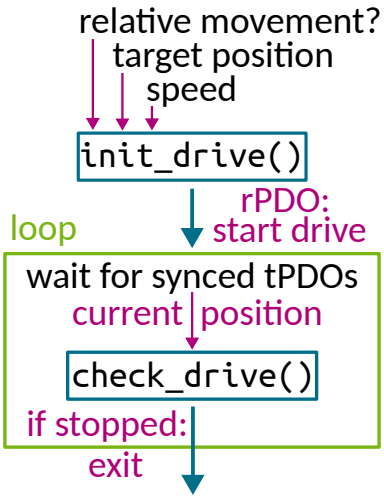

Figure 6.2: Block diagram of the drive process.

First, the target position and the profile velocity are send to the node with rPDOs (receive PDO). The drive is started by switching a bit in the *Controlword*, which also contains the information whether the target position is an absolute or a relative step. This command to start the movement is also transferred to the Motion Controller node via a rPDO.
Afterwards, a loop reads out the tPDO (transmit PDO) which is send by the Motion Controller in time with the synchronization object and contains the current position. A second function then checks whether the drive has been completed and stops the loop if this is the case or the movement has been stopped unintentionally.
During the determination of the wire position the tPDO containing the output signal of the sensor is also read out and stored along the position information.

Valve The solenoid valve that generates the air blast for deflecting the wire for the tension measurement is also connected to the Motion Controller.

```
def valve(self, t_open=0.013):
    Open, Close = 0xFC, 0xFD
    self.node.sdo['Digital I/O status'][4].raw = Open
    time.sleep(t_open)
    self.node.sdo['Digital I/O status'][4].raw = Close
```

Listing 6.2: Function to operate the air valve using the digital outputs of the Motion Controller.

The valve is opened and closed with the function in listing 6.2, which also shows the use of Service Data Objects. The solenoid is connected to the first digital output of the Motion Controller. The object to activate it is stored in the Object Dictionary at the index `0x2311` under the name `Digital I/O status` with subindex 4 (`Write digital outputs`). To open the valve the object is set to `0xFD` which deletes the digital output of DigOut1, but does not change the digital output of all others. The air blast should take $13\,\mathrm{ms}$ [Got05][Ese18]- and afterwards the solenoid is closed again by setting the same object to `0xFD`, which sets the digital output of DigOut1 again.

6.3 Sensor Module

To transmit the output signal of the reflection sensor on the CAN network an Analog Digital Converter (ADC) with a CANopen interface is used. This sensor module (Micro Control µCAN.1.ai-SENSOR / Voltage) is connected directly to the sensor and also powers it. For this reason, the corresponding network node is sometimes also referred to as the sensor in the following.
For such measuring devices there is also a standardized device profile (CiA404), but it is much less complex than that for the Motion Controller. Thus, the NMT commands are sufficient for connecting and activating the sensor module.
During switch-on, only the emergency callback needs to be activated and the PDO mapping needs to be changed slightly in order to achieve synchronous transmission of the voltage signal.

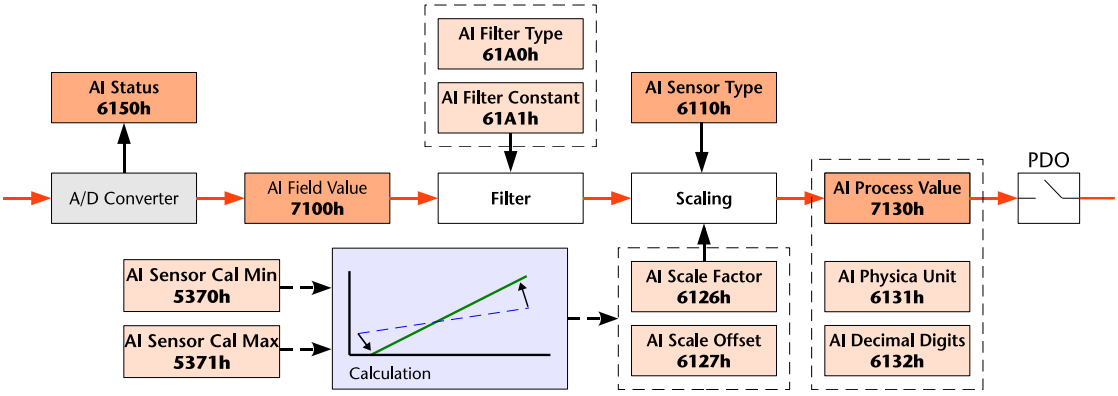

Figure 6.3: Block diagram of the supported functions for the sensor input [Micro].

The functionality of the device profile focuses on handling the voltage signal, as shown in figure 6.3, where the different filtering and scaling functions are displayed together with the OD index of the corresponding objects. First, the sensor signal is digitized by the actual ADC and output as a field value. Then a data filter can be applied ("moving average"), whereby each measured value is processed with the previous one and a filter constant. In regard to the WTTD the exact values at any time are relevant and therefore the filtering is turned off. In the next scaling step, the sensor type is entered (voltage in this case).
Manual scaling can also be carried out, for which a calibration function is provided. To use this, two known values must be applied to the sensor module. These should be at the limits of the maximum value range so that everything is completely covered. The scaling factor and offset are then determined automatically.
Finally, the process value is generated, which is then also transmitted as a message (PDO). This requires the unit and the decimal places, whose values from the object dictionary must be known to all relevant participants on the bus, as the value itself is transmitted as an integer.

If the synchronization of the PDOs is ensured, the value of the sensor signal can be read out at the same time as the position if the query happens within the loop shown in figure 6.2.
The aim of the next chapter is to find out to what extent the components used are suitable for this and for the functionality of the WTTD in general. How the readouts can be implemented efficiently will also be considered.

7 Results

7.1 Characterization of the Components

7.1.1 Linear Drive

In order to determine the exact position of the wires and to be able to precisely navigate to them, the position of the linear drive must be known and reproduced precisely.
For $1\,\mathrm{cm}$ propulsion $2 \cdot 3$ revolutions of the motor are needed, as the corresponding spindle has a pitch (lead) of $5\,\mathrm{mm}$ and the gear converts three motor revolutions in one revolution of the threaded spindle. The encoder that is additionally connected to the motor as shown in figure 5.3 has 4096 increments per revolution. Consequently a resolution of

$$2 \cdot 3 \cdot 4096 \,\frac{\mathrm{incr}}{\mathrm{cm}} = 2.4576 \,\frac{\mathrm{incr}}{\mu\mathrm{m}} \quad \Rightarrow \quad \Delta y = 0.4069\,\mu\mathrm{m}$$

can be achieved. Therefore, the forward accuracy should be less than one micrometer. Nevertheless, the smallest possible steering step with which the position can be read out and commanded is exactly one micrometer. However, this is five times more precise than previous devices [Got05].

7.1.1.1 Internal Position Deviation

There is a function within the Motion Controller matching the current position with the target position by means of a control loop. However, since a micrometer step does not correspond exactly to a multiple of the increments, this process can cause deviations. To prevent this, the movement task is additionally nested in a loop as shown in figure 6.2. This uses the `check_drive()` function, that compares the internal position with the target value. This made it possible to ensure that after the drive came to a controlled stop, **the internal position always corresponds exactly to the required target position**. However, sometimes the motor does relax

a little after being stopped again, leading to deviations from the targeted encoder and position value, if those values are read out after the movement has stopped. To determine the position deviation of the internal values the carriage is driven 100 times along the longest possible way of $120\,\mathrm{cm}$ and the encoder value with the position at the rear end of this drive is queried with an SDO.

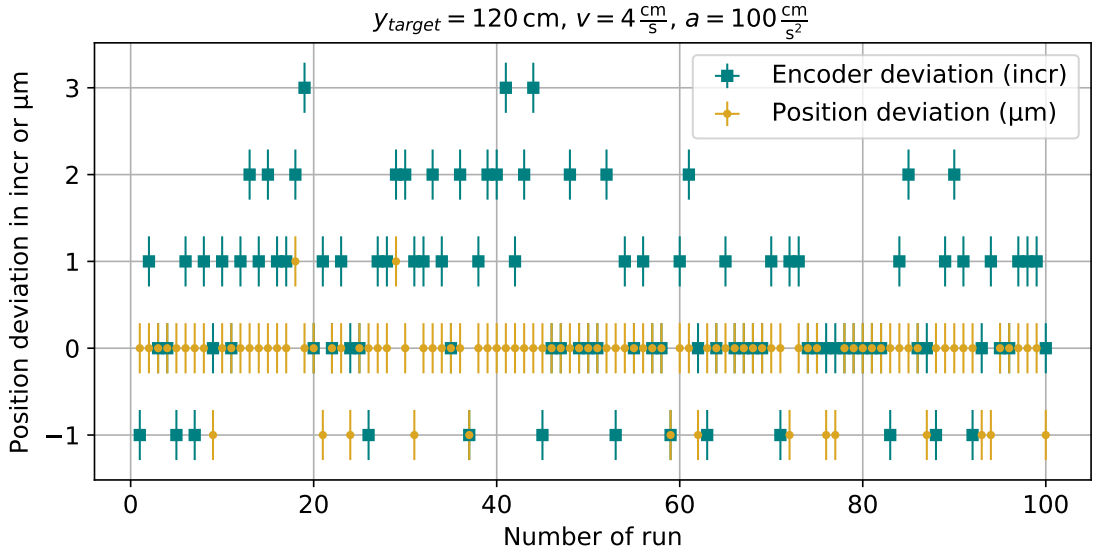

Figure 7.1: Deviation of the internal position and encoder value from the targeted one during 100 runs on the end of a $120\,\mathrm{cm}$ drive.

The deviations from the targeted values are shown in figure 7.1. A discrepancy of the encoder value and the calculated was observed of up to three increments, while the controller still considers proper matching of the position (see run 19). In the same way, the deviation of the encoder can also only equal $2\,\mathrm{incr}$ and the position also deviates by $1\,\mu\mathrm{m}$ (run 18) or it may not (run 40).

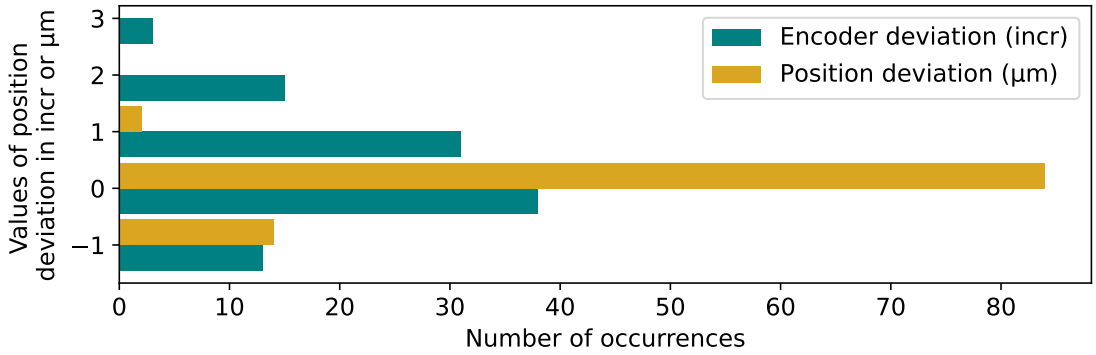

Figure 7.2: Histogram of the encoder and internal position deviation for 100 runs without an additional control loop.

Overall, the encoder value deviates upwards more frequently than downwards or not at all, leading to a positive mean deviation $\overline{\Delta y}_{\mathrm{rep,enc}} = (0.6 \pm 0.1)\,\mathrm{incr}$. The

histogram in figure 7.2 also reveals, that the calculated position most often shows no deviation and deviates downwards more frequently than upwards, therefore the mean value $\overline{\Delta y}_{\mathrm{rep,pos}} = (-0.12 \pm 0.04)\,\mu\mathrm{m}$ is negative and smaller in amount.

As this deviation is monitored in the internal values, the drive can be repositioned. However, to prevent further deviation from occurring due to the reversing play of the components, it is advisable to implement each movement in a movement task. In this way the loop does ensure the correct position and the motor is not stopped, preventing the deviation. As explained in the following chapter, the actual precision of the position measured external, is sufficient for the tasks of the WTTD. Therefore, no further investigation was carried out into how exactly the control and conversion of the encoder values takes place internally in the Motion Controller, leading to the deviation of up to $3\,\mathrm{inc}$.

7.1.1.2 Position Precision

In order to prove the precision of the linear drive, the position is also measured externally. To do this a dial gauge is attached to the linear drive on whose plunger the measuring slide touches. The available dial gauge (Käfer GM100) has a precision of $0.01\,\mathrm{mm}$. This is sufficient because the precision of the linear drive has to be in the order of the wire diameter of which the smallest is $0.02\,\mathrm{mm}$.
Furthermore, the analogue scale still enables a slight level of interpolation. If the total deviation at the end is within one scale line, the precision is sufficient.
For an even more accurate length measurement, which can confirm the $1\,\mu\mathrm{m}$ internal precision, the overall conditions would also have to be adjusted. If a $1\,\mu\mathrm{m}$ accurate dial gauge were to be used, it must be ensured that deviations could not be caused by the stiffness of the fastening or thermal expansion, for example.
With this dial gauge, the uncertainty is calculated from the triangular distribution of a scale line (see appendix D), but the actual read-off takes place on a quarter scale division: $2.5\,\mu\mathrm{m}$.

After all, it is important that a position is not only read out accurately, but also moved to precisely and repeatably. To ensure this, a hysteresis movement sequence is run where the measuring carriage moves in fixed steps in one direction and then back again.

Relative Steps As the wires have to be controlled precisely one after the other to measure the wire tension, relative steps of the same increment are used initially. In a first test, 40 steps with a step size of $10\,\mu\mathrm{m}$ should be carried out.

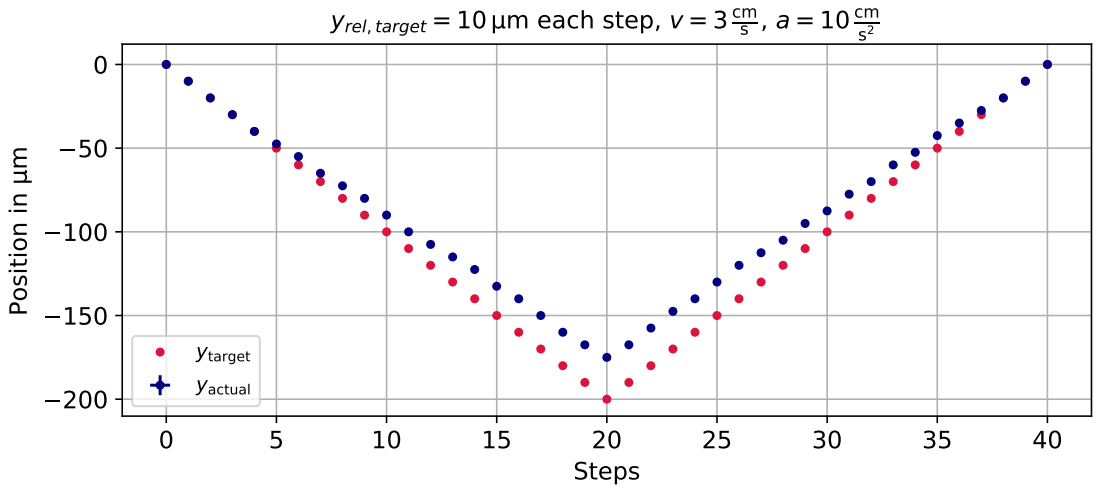

Figure 7.3: Position measured width the dial gauge of 40 relative steps with a step size of $10\,\mu m$ and the targeted position.

The diagram in figure 7.3 shows that the steps are not as wide as they should be. Therefore, the reversal point is not at $-200\,\mu m$, where it is supposed to be, but is reached $25\,\mu m$ sooner. However, the step width ($\overline{\Delta y}_{\text{relative}} = (8.9 \pm 0.1)\,\mu m$) is constant on average, which is why the starting point is reached again after the same number of steps have been taken back. As can be seen in figure 7.4 on the left, the sum of the first 20 deviations is therefore just as large as that of the following 20 values.

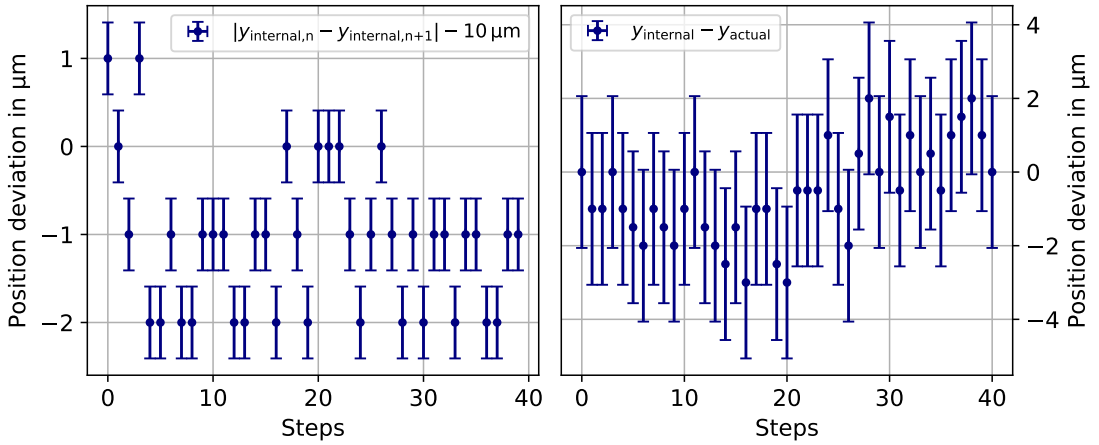

Figure 7.4: Left: Deviation of the internal monitored step with from the commanded one.
Right: Difference between the internal and actual position.

Figure 7.4 on the right shows that the difference between the internal monitored and the actual steps are very small compared to the $25\,\mu m$ maximum deviation and do not show the same behavior of the total deviation, which first increases and then decreases again. The uncertainty bar for almost every value intersects the 0-deviation line. Regarding the values where this is not the case, this may also

be due to the difficulty of reading the scale within a quarter of a scale mark. Overall, this means that the Motion Controller has knowledge of the incorrect step size during the relative movement. The fact that the positions are not reached correctly may be due to a faulty control loop for relative steps. It is therefore first checked whether these deviations also occur if the steps are each passed as a movement task to an absolute position.

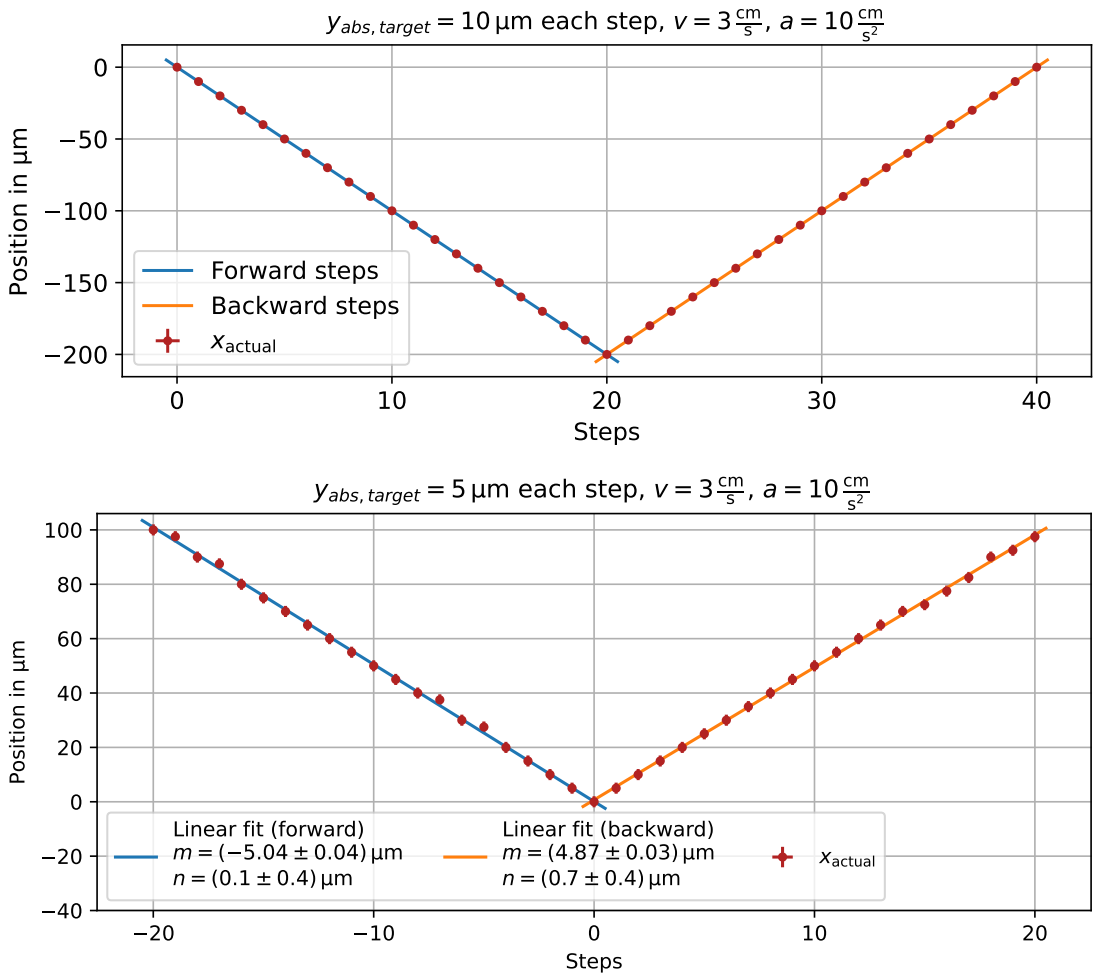

Figure 7.5: Position measured with the dial gauge of 40 steps with a step size of $10\,\mu m$ (top) and $5\,\mu m$ (bottom), executed as movements toward absolute positions.

Absolute Steps Are the $10\,\mu m$-steps commanded as movements towards absolute positions there is no deviation. Figure 7.5 shows, that the position values are exactly on the expected lines for the forward and backward movement. This pattern is also confirmed by multiple measurements with this step size over longer distances. **This ensures that the precision of the linear drive is in the range below $10\,\mu m$, which means that wires can be approached precisely.**

Reversing Play For smaller step widths, such as the $5\,\mu m$ steps displayed in figure 7.5 some deviations occur. These could be caused by incorrect reading, as they are exactly $2.5\,\mu m$ if they appear. This could also be related to the reversing play, which is another important factor in regard to the precision of the linear drive. The rotation of the motor is transferred via a gearbox and a coupling to the threaded spindle, on which the carriage moves, using a ballscrew drive. All these mechanical components will have a certain amount of play. If the direction of rotation changes, this play must first be cleared before the carriage also changes its direction of movement.

If a linear fit is performed with the data, according to $y = m \cdot s + n$ where y is the position and s the steps, the reversal play can be determined from the axis intercepts n. In the case of the $5\,\mu m$ steps displayed in figure 7.5 (bottom), the difference between the axis sections is $\Delta n = (0.6 \pm 0.6)\,\mu m$. The inaccuracy in this value is difficult to reduce as the step size has a lower limit. In addition, multiple measurements were not carried out, as the deviations that lead to a non-zero axis intercept in the first place can also be caused by incorrect reading of the quarter scale steps. Furthermore, a deviation at the reversal point itself was never observed in several measurements with this increment.

In order to determine the reversing clearance more precisely, another measuring method is used. A certain position is reached and from then on the carriage is moved back in micrometer steps until the pointer of the dial gauge moves for the first time, because then the backlash has been exceeded. However, it is difficult to give an exact measured value. A measurement with 50 repetitions shows that on average the reversing play is $\Delta y_{\text{rev}} = (4.13 \pm 0.09)\,\mu m$. However, if steps with a size of $4\,\mu m$ or even $3\,\mu m$ are carried out, it is not the case that the indicator would not move at all during the first step. This also shows the lack of a deviation at the reversal points of the step measurements with larger step widths as shown in figure 7.5 and the small value of Δn. Nevertheless, for step sizes close to the average value calculated before, it can be observed that the first step is smaller than the following steps. However, this cannot be quantified with the dial gauge provided, but in any case it has been shown that **the reversing play is also sufficiently small, due to its value being less than one hundredth of a millimeter**. The differences in the value of the backlash for different step sizes may be due to the fact that with each stop the mechanics relax slightly and with each new acceleration this clearance must be overcome as well. It is therefore recommended that the scan for the wire position is made with one run without a break and that the wires for the tension measurement are reached with just one step at a time.

If it is necessary to determine the position accuracy even more precisely, for example because it turns out that the focal point should be exactly in the center of

a wire for an accurate reflection measurement, the measuring method should be changed. A more precise dial gauge is ruled out for the reasons mentioned above; instead, a laser distance measurement should be carried out. The measuring device itself should not be connected to the linear drive, but a constant distance should be ensured between them.

7.1.1.3 Repeatability and thermal Expansion

When operating the WTTD, it is important to ensure precision also for movements covering the entire length of the linear drive. It is also crucial to ascertain the extent to which high travel speeds, which would facilitate a rapid scanning process, influence the accuracy of the results.
The ballscrew drive, which moves the carriage across the spindle, does also heat it up due to friction. If the speed of movement is higher, this results in greater heat and, because of the relatively long length of the spindle, the expansion becomes measurable. The spindle can expand freely as one side has a fixed bearing and the other a floating bearing.
It is not possible to measure the exact temperature of the spindle due to its length. However, the Faulhaber motor has a temperature sensor and even tough there is no connection between the two quantities it is still the best accessible value. Furthermore, it can be assumed that the spindle and motor heat up similarly in relative terms, as both heat-ups are speed-dependent.
For the measurement of the position repeatability the carriage is driven back and forth $120\,\mathrm{cm}$ and the position as well as the motor temperature is measured at the end of this drive. Before setting a new speed, it has been ensured that the motor is cooled down to the initial temperature of $22\,^{\circ}\mathrm{C}$ again.

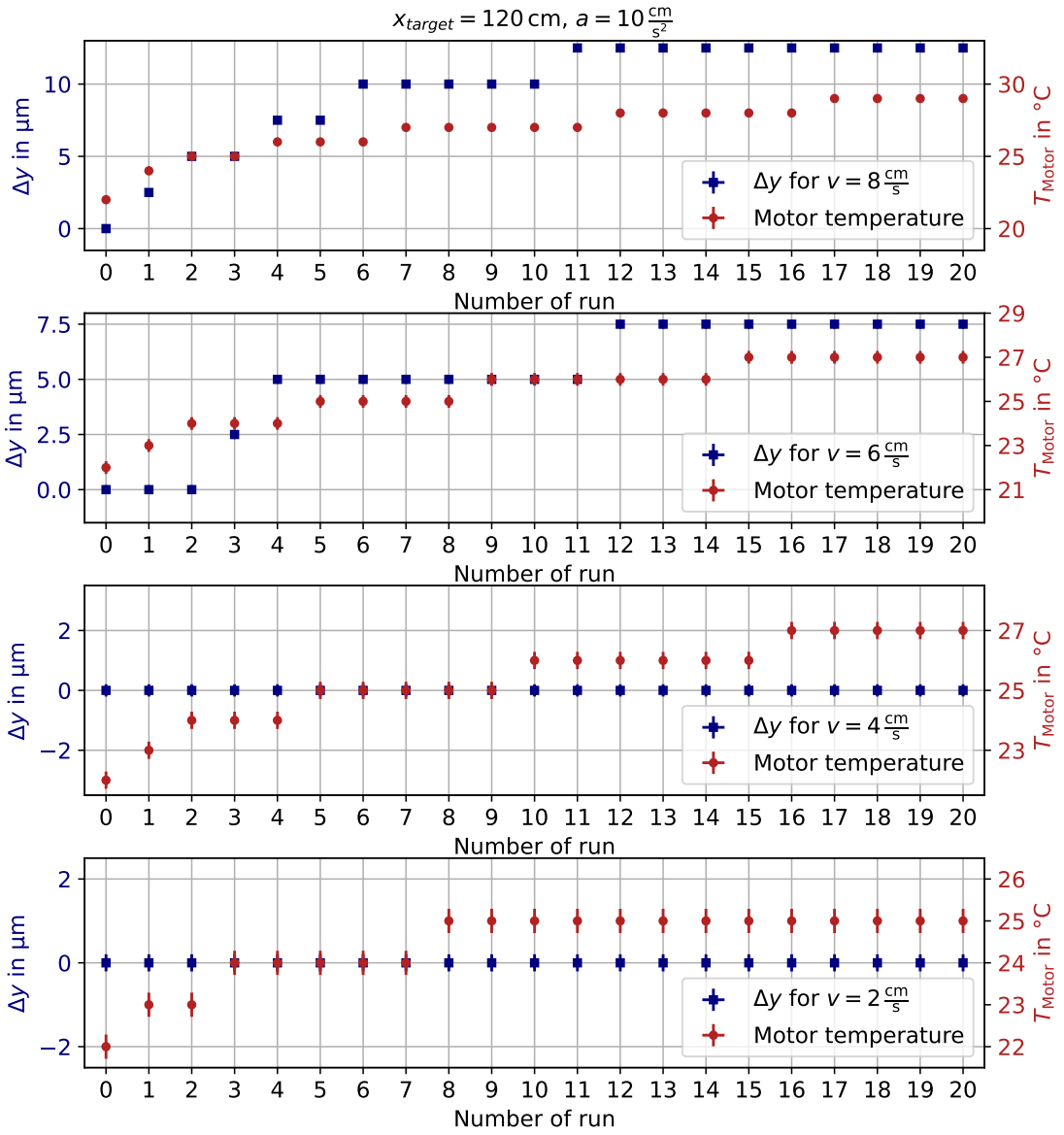

Figure 7.6: Position deviation and motor temperature at the end of a drive completing $120\,\mathrm{cm}$ forward and backward. Results based on 20 runs and four different velocities.

As shown in figure 7.6, the deviation of the position increases for high speeds after a drive twice $120\,\mathrm{cm}$ long. This result can be described with the thermal expansion of the spindle.

The material used for the spindle is Cf53 steel (EN steel number 1.1213) an alloyed carbon steel with $0.53\,\%$ carbon. According to the manufacturer of the linear drive and [ASM02, p. 58] the linear thermal expansion coefficient of this steel is $\alpha = 11.5\,{}^{1}/_{\mathrm{K}}$. With the entire length of the spindle $l = 1300\,\mathrm{mm}$ and the maximum position deviation of $\Delta y = (12.5 \pm 0.2)\,\mu\mathrm{m}$ the rise in temperature would be:

$$\Delta T_{\mathrm{spindle}} = \frac{\Delta y}{\alpha \cdot l} = (0.83 \pm 0.01)\,\mathrm{K}$$

This heating is significantly less than the one measured in the motor, where heating also occurs due to the electrical currents in addition to friction. The large surface area of the spindle also means that the heat can be dissipated much more efficiently. This has the effect that there is no thermal expansion at speeds of $4\,{}^{\mathrm{cm}}/_{\mathrm{s}}$ and below. If the drive moves slowly, the heat is dissipated quickly enough so that there is no net heating.

It is therefore important during operation of the WTTD that a maximum speed of $v_{\max} = 4\,{}^{\mathrm{cm}}/_{\mathrm{s}}$ is not exceeded. This is still 2400 times higher than the minimum supported speed of $v_{\min} = 1\,\mathrm{mm/min}$.

Regarding the scan of the wire position, the speed used is derived from the total measuring time manageable. In order to achieve this, it is necessary to ascertain the rate at which data is transmitted to the network, what is the focus of the next chapter.

7.1.2 Motor and Sensor Network Speed

In order to achieve a synchronized read out of the position and the reflection value the master sends out SYNC pulses with the frequency f_{N}. Each node stores its respective measured value at the time it receives a SYNC message. Furthermore, both nodes are configured to reply to every pulse with a PDO message containing this latest value.

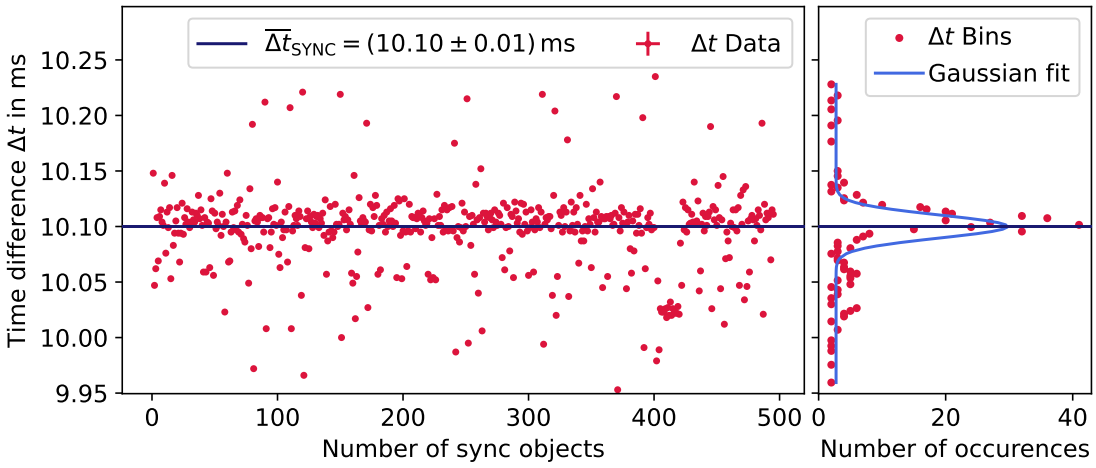

Figure 7.7: Diagram of the time difference between every two consecutive sync messages. The histogram for the different values is displayed rebinned by a factor two and fitted with a Gaussian peak on the right.

To determine the precision of this synchronisation the messages on the bus for 500 SYNC messages at a frequency of $f_{\mathrm{N}} = 100\,\mathrm{Hz}$ are analysed. The messages were monitored (`candump`) and the time difference between the messages (time of arrival at the master) is calculated.

Although the SYNC pulses are sent by the master itself with the fixed frequency $f_N = 100\,\mathrm{Hz}$, the values for the time difference between the successive messages fluctuates, as can be seen in figure 7.7.

The mean value $\overline{\Delta t}_{\mathrm{SYNC}} = (10.10 \pm 0.01)\,\mathrm{ms}$ is larger than the expected $1/f_N = 10\,\mathrm{ms}$. This may be due to a processing time between the SYNC impulses being commanded by the script and their actual transmission. In addition to this discrepancy, there is a standard deviation of $\sigma_{\mathrm{SYNC}} = (0.010 \pm 0.002)\,\mathrm{ms}$, due to the fluctuations.

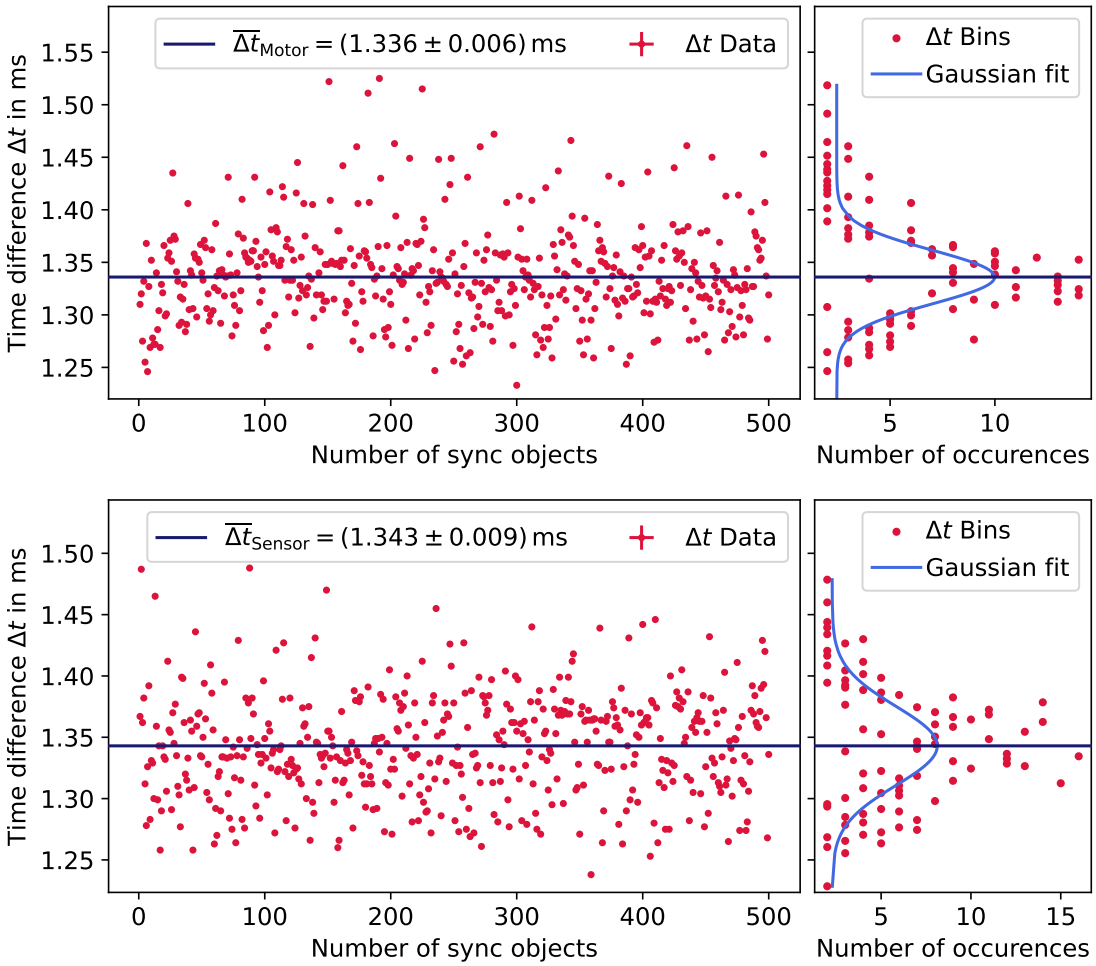

Figure 7.8: Diagram of the time difference between the sync message and the responding PDO of the Motion Controller (top) and the sensor module (bottom). The histograms are displayed rebinned by a factor two and fitted with a Gaussian peak on the right.

The standard deviation was determined by performing a data fit (weighted sum of squared residuals) in `fityk` using a Gaussian function. The fluctuations could be caused by delays in the calculation of the commands. In particular, the scheduling of the send processes in the kernel must be taken into account. However, the size

of the fluctuation is in a typical order of magnitude but could be reduced if the process is executed on a real time kernel.

If the time difference between the PDOs sent in response to the sync pulse and the sync pulse is calculated, the result is the distribution as plotted in figure 7.8. The fluctuations become larger as processes also run in parallel on the nodes:

$$\sigma_{\text{Motor}} = (0.025 \pm 0.006)\,\text{ms}, \qquad \sigma_{\text{Sensor}} = (0.03 \pm 0.01)\,\text{ms}.$$

Nevertheless, as the order of magnitude does not change, these fluctuations are acceptable, because they are just around 2% of the respective time difference. Therefore, they do not cause interference of the different messages.
However, it is the mean value of the time differences which results in a limiting factor. Both the motor and the sensor PDO are received approximately $1.34\,\text{ms}$ after the sync pulse is sent. This value is due to the fact that an eight byte long message at a transmission rate of $f_{\text{bit}} = 1\,\text{Mbit/s}$ itself already has a length of $0.064\,\text{ms}$. The sync pulse must be sent to the node, processed there and the PDO sent back, which in addition to the fact that messages cannot be sent in parallel results in the runtime value. From the reciprocal of this runtime, a sync frequency of approximately $f_{\text{N}} = 750\,\text{Hz}$ is considered achievable, without disturbances.
Only if the PDOs follow the fixed sequence, with the sync pulse (COB-ID 080) first and then the responses from the field devices, it is possible to ensure that the measurements are synchronized. This is due to the fact that no information on the time of measurement can be transmitted in the PDOs and no uniform counter is supported by both devices.
For the motion controller, this sequence remains the same up to a synchronization frequency of $f_{\text{N}} = 725\,\text{Hz}$ close to the previously calculated one.
This is not the case in regard to the sensor module where, even at frequencies above $f_{\text{N}} = 400\,\text{Hz}$, it is possible that no response is received between two sync pulses and thus the sync sequence is lost. **Using the current ADC, the speed of reading out the measuring devices is therefore limited to this frequency.** However, a frequency of $f_{\text{N}} = 400\,\text{Hz}$ is not sufficient because the resulting Nyquist frequency is smaller than the fundamental frequency of the anode wire in a small chamber (see table 4.2). This oscillation could therefore not be reconstructed from the measured data.
The network frequency supported by the Motion Controller combined with the traversing speed results in the resolution for scanning the wire positions. This must finally be optimized in real operation, which is possible down to $1\,\mu\text{m}$ positioning step. To achieve exactly this resolution at $f_{\text{N}} = 700\,\text{Hz}$ it would require a velocity of $v = 0.07\,{}^{\text{cm}}/_{\text{s}}$, leading to a scan duration of about 20 minutes for one wire plane

(large chamber). As this is a reasonably short period of time and the precision of the movement is sufficient as described above, **the linear drive is suitable for the tasks of the WTTD**.

7.1.3 Sensor

The reflection sensor (OMRON *EE-SPY402*) includes both a GaAs infrared LED ($\lambda = 940\,\mathrm{nm}$) and a photodiode to detect the reflection. This sensor was picked as a first test, but **the sensor only has a digital output** (NPN). It is therefore not possible to make a statement about the strength of the reflection, but only to determine whether a reflection is present or not. With that it is still possible to determine the position of the wires. Depending on the spatial resolution used, the center of the wire could be determined from the center of a plateau when there is reflection. However, to determine the tension, the wire would have to oscillate completely out of and back into the focal point of the sensor so that the digital output also changes periodically. As the oscillation amplitudes are small, this cannot be guaranteed.
The sensor is entirely unsuitable because **the reflection on a single wire cannot be detected**. To verify this, the sensor was positioned exactly at the specified focal length of $5\,\mathrm{mm}$ above a tensioned wire using the fine drive. The sensor was then moved over the wire with the lowest possible speed of $1\,\mathrm{mm/min}$, but there was not a single reflection.
This measurement was carried out for the thicker cathode wire and the sensor did not detect a reflection until the wire was folded twice, making it four times the diameter. To solve this problem, a lens could be manufactured that sits in front of the sensor and increases its magnification. From the resolution achieved currently to one that also recognizes the $20\,\mu\mathrm{m}$ thin anode wires, the magnification would then have to be improved by a factor of 15. Even if this were possible, the problems resulting from the fact that the sensor does not provide an analog signal of the reflection strength would still remain. The measurements are not possible with the current sensor. Instead, the sensor module (ADC) is characterized in more detail below.

7.1.4 Sensor Module

Instead of attaching the sensor voltage signals from a power source or a sine generator have been applied to the sensor module. These have a voltage range from $-10\,\mathrm{V}$ to $10\,\mathrm{V}$.

7.1.4.1 Direct Current Measurements

First, a DC voltage with $0.5\,\mathrm{V}$ steps within this range is applied. For each applied voltage the mean value of 2000 samples is calculated.

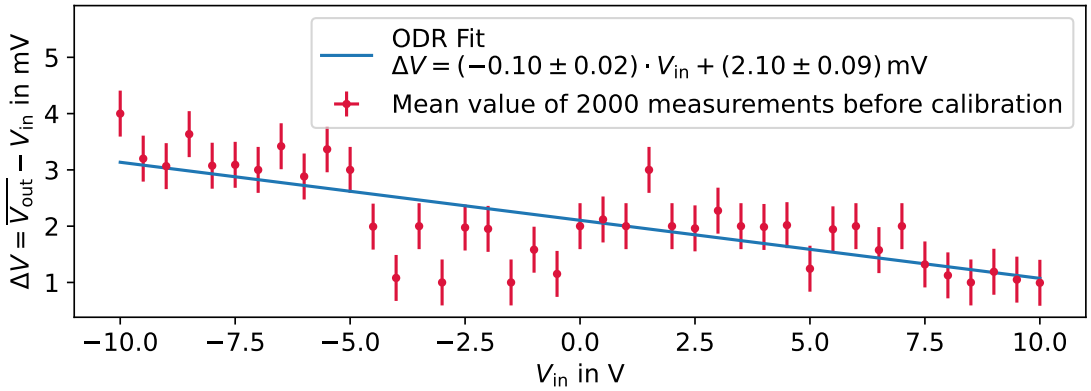

Figure 7.9: Difference between voltage applied to the sensor module and the mean measured value for different voltages over the whole supported range.

In figure 7.9 the difference between the applied voltage and the measured one is displayed. The deviation is the greatest on the minimum of the range and decreases with rising voltages applied. A linear fit ($\Delta V = m \cdot V_{\mathrm{in}} + n$) is therefore performed using *scipy.ODR* (least squares fit). Despite the slope of $m = -0.10 \pm 0.02$, the deviation does not reach zero at the end of the supported voltage range. Additionally the values are fluctuating around the trend line. A reason for this could be uncertainties in the sensor module or fluctuations and deviations in the power supply, especially since mV are the smallest values that the power supply can deliver. In order to reduce the differences the calibration process implemented in the CiA404 standard is performed with a voltage of $-10\,\mathrm{V}$ and $10\,\mathrm{V}$. After this re-calibration the same voltage measurements are done, whose deviations are shown in figure 7.10.

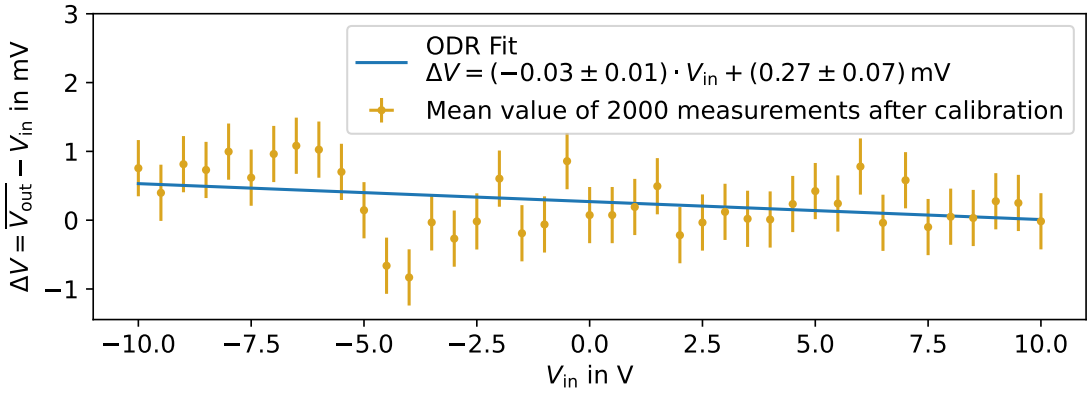

Figure 7.10: Difference between voltage applied to the sensor module and the mean measured value after the re-calibration.

After the re-calibration the values measured differ less. Nevertheless, the trend of falling values can still be seen, which could be due to the ADC's non-linear measurement behavior. The calibration was therefore not complete. However, especially for positive values, the deviation is very small and even reaches zero at the end of the range. Overall, the differences are less than $\pm 1\,\mathrm{mV}$, which means that they on average transmitted correctly with the three decimal places of the PDO.

7.1.4.2 Dynamic Signals

Both the signal during the scan of the wire position and that of the voltage measurement are not constant. It is therefore important to analyze the sampling of the sensor module.

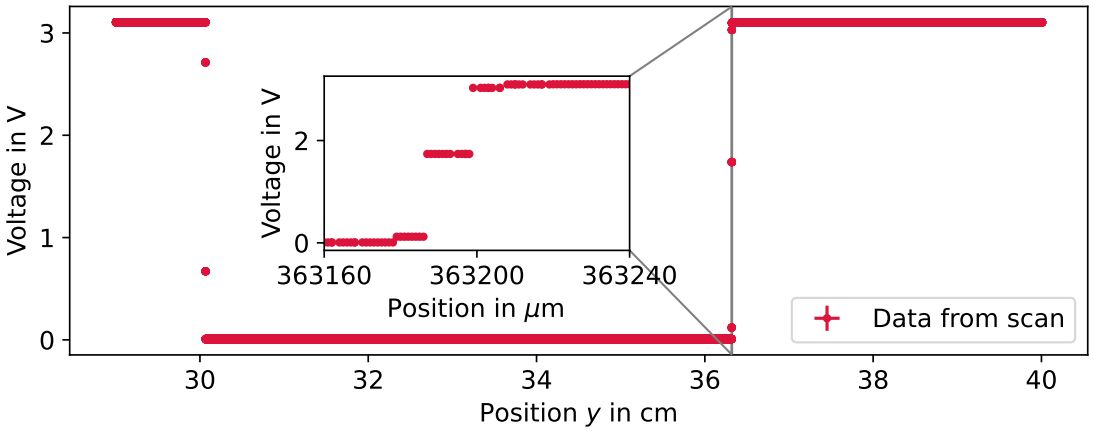

Figure 7.11: Voltage signal from the sensor module during the drive along a reflecting block positioned between the coordinates $y = 30\,\mathrm{cm}$ and $y = 36.3\,\mathrm{cm}$.

If the sensor module with the sensor attached is moved across an edge of a reflecting material the signal measured follows as displayed in figure 7.11. The digital output of the sensor is "normally on" (NO), so during the detection of an reflection the output drops to zero.

Looking closely at the edge in the values, it is noticeable that there are intermediate values. However, these are not possible with a digital output that can only accept two possible values. They must therefore originate from the sampling of the ADC.

To investigate these intermediate values further, a square-wave signal is applied to the ADC without the sensor and this is recorded with the ADC.

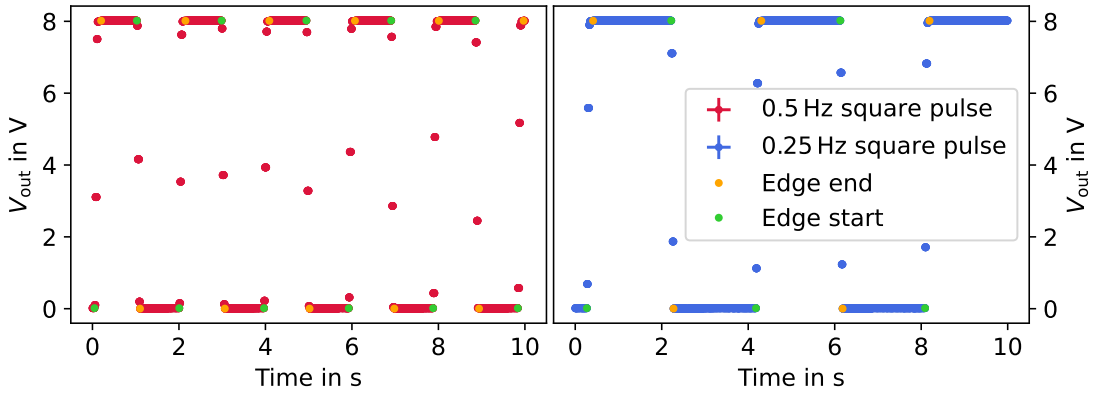

Figure 7.12: Voltage signal from the sensor module with a $0.5\,\mathrm{Hz}$ and a $0.25\,\mathrm{Hz}$ square pulse applied.

In figure 7.12 the output of the ADC at a network sync rate of $f_\mathrm{N} = 400\,\mathrm{Hz}$ is displayed and the intermediate values can also be seen in the rising and falling edges. To determine the length of the rising and falling edges, the data points at the beginning and end of each edge are selected. These are characterized by the fact that they differ more from the predecessor or successor than in the noise of the plateaus and are above respectively below a certain threshold value. The length of the edges are:

$$t_\mathrm{Edge}(0.5\,\mathrm{Hz}) = (0.11 \pm 0.01)\,\mathrm{s}, \qquad t_\mathrm{Edge}(0.25\,\mathrm{Hz}) = (0.09 \pm 0.02)\,\mathrm{s}.$$

The same method was used to determine the length of the edges of the input signal. This was sampled with an oscilloscope at a frequency of $2\,\mathrm{GHz}$. The edge length here is only $t_\mathrm{Edge} = (17.9 \pm 0.2)\,\mathrm{ns}$, which is also in accordance with the manufacturer's specification of $t_\mathrm{Edge} \leq 18\,\mathrm{ns}$ [Tek12]. This means that no edge should be visible at all with the ADC sampling rate. Despite the fact that filtering is switched off according to the CiA404 standard, these intermediate values occur as if there were some averaging in the sensor module.
This also means that the plateaus of the rectangular pulses are shortened. The relative deviation to the actual length is:

$$\Delta T/T(0.5\,\mathrm{Hz}) = (-13 \pm 1)\,\%, \qquad \Delta T/T(0.25\,\mathrm{Hz}) = (-7 \pm 1)\,\%.$$

This causes the amplitude of signals which have a periodicity in the range of the edge duration not to be displayed correctly. This is due to the nature of the discretization of signals. The sampling itself is done mathematically with a rectangular pulse. This means that in the frequency domain, the Fourier transform of a rectangular pulse is folded with the Fourier transform of the signal.

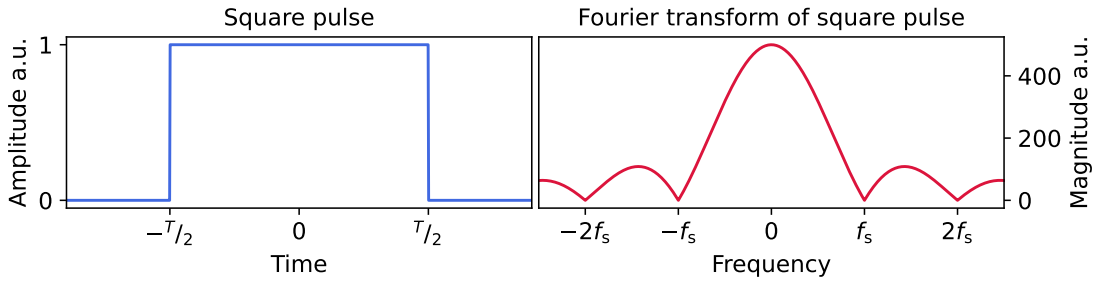

Figure 7.13: Square pulse signal and its Fourier transform a sinc-function.

The absolute value of the Fourier transform of a square pulse is shown in figure 7.13. On the one hand, it can be recognized that because periodic signals repeat in frequency space at multiples of the sampling frequency $f_s = 1/T$, these would overlap if the sampling frequency is not twice the signal frequency. On the other hand, one can also see how the magnitude of the Fourier transform decreases for increasing frequencies towards the sampling frequency. However, signals with steeper edges have higher frequency components, and their magnitude is attenuated by the shape of the sinc function.

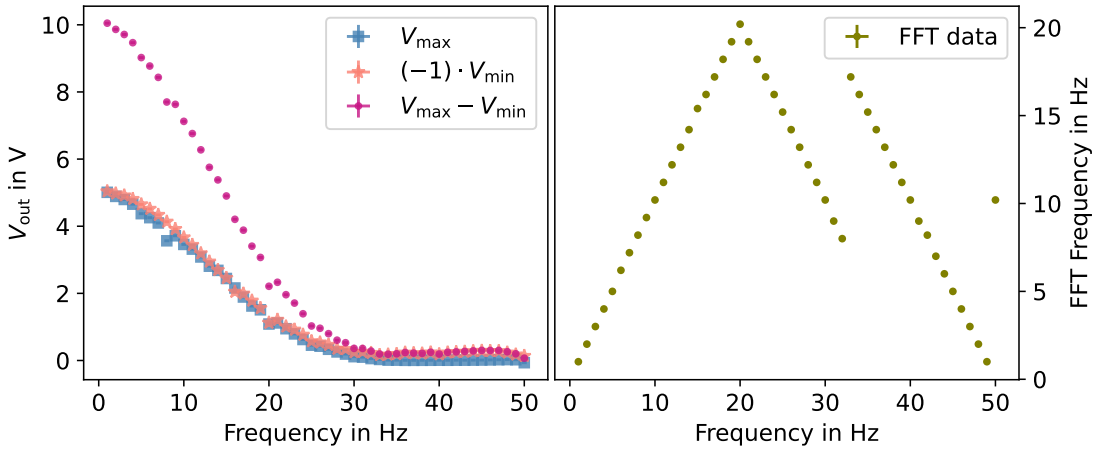

Figure 7.14: Amplitude (left) and determined frequency (FFT) for sine waves of rising frequency.

In order to determine the sampling rate of the sensor module, a sine wave is applied to it and recorded for $5\,\mathrm{s}$ with a network frequency of $f_N = 400\,\mathrm{Hz}$. This is repeated for signals with a frequency of $1\,\mathrm{Hz}$ to $50\,\mathrm{Hz}$ and a voltage between $-5\,\mathrm{V}$ and $5\,\mathrm{V}$.

As the frequency increases, the sensor module only records smaller and smaller differences in the voltage. This decrease in amplitude is shown in figure 7.14 on the left-hand side. Both the minimum voltage, which should be $-5\,\mathrm{V}$, and the maximum voltage, which should also be the same for each signal at $5\,\mathrm{V}$, approach $0\,\mathrm{V}$ with increasing frequency. This is due to the steeply falling edges of the sinc

function, mathematically describing the sampling. In order to determine the frequencies precisely, a Fast Fourier Transform is performed. The function that will be used in the future to detect the fundamental frequency of the wires is used for this. In figure 7.14 on the right-hand side, the result of the FFT is shown for the increasing frequencies that are applied. First, the values increase and the values determined with the FFT correspond to the actual ones. From $20\,\mathrm{Hz}$, there is undersampling and the frequencies are folded back into the frequency range below the Nyquist frequency, causing the frequencies determined by the FFT to decrease again. The same pattern is visible if the measurement is repeated with square wave pulses.

Starting at a frequency of $33\,\mathrm{Hz}$, the peak of the first alias frequency at $7\,\mathrm{Hz}$ is so low that it can no longer be distinguished from the noise. Therefore, the frequency appears at the next higher frequency following equation (4.24) of $17\,\mathrm{Hz}$. The frequencies then continue to decrease until at $50\,\mathrm{Hz}$ the next periodic alias is the one with the highest magnitude, which appears at $10\,\mathrm{Hz}$.

Since the FFT frequencies drop again from $20\,\mathrm{Hz}$ and the following values can be identified as aliases according to equation (4.24) at a Nyquist frequency of $f_{\mathrm{Nyquist}} = 20\,\mathrm{Hz}$, **the sampling frequency of the ADC can be specified as** $f_\mathrm{s} = 40\,\mathrm{Hz}$. This value is not sufficient to achieve the expected fundamental oscillation (see table 4.2). This means that the sensor module used is also not suitable for this purpose. In communication with the manufacturer, this could be traced back to a mismatch in product specifications. A replacement board, which should achieve a sampling rate of $f_\mathrm{s} = 1\,\mathrm{kHz}$, is expected to be delivered soon.

The motion controller has proven to be adequate overall. Therefore, the sampling frequency as well as the maximum synchronization frequency of a new sensor module should reach a value of $f_\mathrm{N} = f_\mathrm{s} = 725\,\mathrm{Hz}$ to be equivalent to the MC.

As the ADC communicates solely on the network to determine the wire tension, the frequency could be increased for this measurement. This could be necessary due to the fact that in addition to the fundamental oscillations in the frequency spectrum of the wire oscillation, higher harmonics are expected [Got05]. If these frequencies are undersampled, they could be mistaken for the fundamental frequency. In order to correctly reconstruct the amplitudes of higher frequency components, a sampling frequency of $f_\mathrm{s} = 1\,\mathrm{kHz}$ would be desirable. However, a sampling frequency of $f_\mathrm{s} = 10\,\mathrm{kHz}$ as used in comparable setups [Ese18] does not have to be achieved, as higher harmonics are already significantly attenuated at such high frequencies. In addition, a high sampling rate is of limited utility if the network rate f_N is not at least equivalent.

7.2 Measurement Implementation and Simulation

Despite the fact that the components are not yet sufficient for real measurements, the routines for the actual measurement have already been implemented and tested with simulated data.

7.2.1 Wire Position

Regarding the scan of the wire position, it can be assumed that the voltage signal during the reflection of a wire is sufficiently distinct from the background noise. Therefore, **a simple "peakfinder algorithm" is sufficient to determine the position of the wires**. As with the tension measurement, this is implemented using scipy.signal.find_peaks. Depending on the selected spatial and reflection resolution, it may also be necessary to locate the center of the wire from the reflection distribution.

7.2.2 Wire Tension

However, several steps are required to determine the wire tension. First, a frequency spectrum is determined by performing a FFT with the values of the voltage sampled with the frequency f_{N}. Subsequently, the fundamental frequency must be identified in the spectrum. Both steps are described in more detail below.

Fast Fourier Transform The FFT is performed as described in section 4.4.1 with scipy.fft. The highest possible frequency is, according to the sampling theorem, defined by half the rate at which the signal was sampled, which corresponds to $f_N/2$ here. The resolution depends solely on the total duration of the measurement. However, this is limited by the decay of the signal and by the restriction that the total measurement time of all wires should remain within reasonable limits. With 384 wires per plane, two wire planes in the chamber and one measurement each before and after the installation of the wire plane, this time can be significant, even if it seems small individually. In order to optimize the value, the influence of a reduced frequency resolution on the measured tension value is investigated. This is done by Gaussian error propagation with the equation (4.20)[1].
First the sensitivity of the tension to changes in the frequency is calculated by derivating T with respect to f_0:

$$\frac{\partial T}{\partial f_0} = 2\pi\rho f_0 l^2 d^2$$

According to the Gaussian error propagation, the variance of tension caused by the uncertainty in the frequency is derived by multiplying this with the deviation of frequency:

$$\sigma_T = \left(\frac{\partial T}{\partial f_0}\right) \cdot \sigma_f = 2\pi\rho f_0 l^2 d^2 \sigma_f$$

This standard deviation σ_T represents how much the value of the tension is expected to vary due to variations or uncertainties in the frequency.
For this particular purpose, the tension should have a deviation of less than 1%:

$$\frac{\sigma_T}{T} \overset{!}{\leq} 1\%.$$

According to the frequencies in table 4.2 this results in the maximum tolerable frequencies as displayed in table 7.1.

Table 7.1: Maximum frequency deviations σ_f leading to a deviation of the wire tension of less than 1%.

Module type	1 & 3	5 & 7
$\sigma_{f,\text{anode}}$	1.3 Hz	0.8 Hz
$\sigma_{f,\text{cathode}}$	0.8 Hz	0.4 Hz

[1] Note that the Gaussian error propagation gives the standard deviation σ based on the difference between the function values at the input parameter plus and minus its deviation, in order to gauge the spread of the output due to the uncertainty in the input parameter. If the deviation is given in relative terms, this must be done separately for the upper and lower limit, as the deviation is relatively different in size. However, as these are only small deviations, the deviation is also regarded as relatively the same here and only one value is given.

If only the resolution of the frequency spectrum contributes to the deviation ($\sigma_f = \Delta f_{\mathrm{FFT}}$), then the smallest tolerable frequency deviation results in a measurement time in regard to the FFT of $2.5\,\mathrm{s}$. Considering all wires within a plane and a single measurement each, this results in a measuring time for of exactly 16 minutes. The resolution is furthermore comparable, with a present setup, with one of $0.6\,\mathrm{Hz}$ [Ese18, p. 46].
The measurement time is implemented as a time window of the FFT. The actual measurement is started with the deflecting air blast but the FFT is started after the transient phase and stopped before the signal has subsided too much. Moreover, this measurement time is a recordable value for the large chamber [Ese18] and should be achievable for the smaller chambers too.

Detection of the fundamental Frequency After the Fast Fourier Transform is computed the peak for the fundamental frequency must be found. The function provided by scipy.signal.find_peaks is used for this purpose. This function has various properties to define peaks. Additionally a expected frequency is implemented, from which the fundamental frequency is scanned for in a $\pm 10\,\%$ surrounding. To describe the simulated data, it is sufficient to use the prominence of the peaks to distinguish them from the noise. The peak for the fundamental oscillation is the first one, with a non-zero frequency. If no peak in the spectrum meets the requirements of the "peak finder", the frequency is chosen as the one in the given range around the expected frequency that has the highest magnitude. The whole function for the FFT and the detection of the fundamental frequency is given in appendix C.

To test these implementations simulations were performed. These were created in comparison with real data provided by an existing setup [Ese18, p. 46]. The expected signal has a duration of at least $5\,\mathrm{s}$ and an amplitude of about $7\,\mathrm{V}$. The simulated signal is generated in time steps corresponding to the sampling rate.
In order to have a realistic signal, which can probe the limits of the determination method, the underlying signal is superimposed with various types of interference. The complete function generating the simulated signal is given in appendix C. First, there is noise, which has an adjustable ratio to the signal amplitude and a Gaussian distribution. **Up to a noise ratio of about 80% of the signal amplitude, the fundamental frequency is reliably determined.**
Furthermore, the signal is multiplied by a decay that causes the amplitude to drop exponentially to less than one percent within five seconds. Before the actual signal begins, a simplified transient process is also simulated. This is done by adding periodic signals which have a random amplitude and random frequency up to ten

times the signal frequency (Gaussian distribution). The total amplitude of this process increases towards the actual signal amplitude over a duration which can be specified.

Finally, the signal is added with higher harmonics, in other words frequency components with multiples of the fundamental frequency. While the previous parameters have almost no influence on the determination of the fundamental frequency, the higher harmonics can lead to interference. This happens when they exceed the Nyquist frequency and are therefore folded back into the possible spectrum of the FFT. Since the exact proportions of the higher harmonics in the real signal are still unknown at this point, they are initially limited to the Nyquist frequency. As they have a lower strength compared to the fundamental frequency in any case, they could also be filtered using the peak finder parameters. In figure 7.15 a signal simulated in this way is shown for the oscillation of the cathode wire in the small chamber at a sampling rate of $400\,\mathrm{Hz}$.

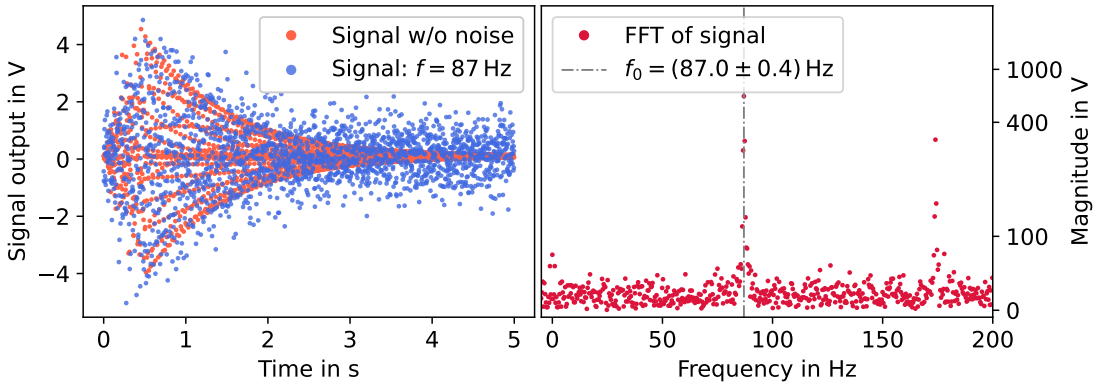

Figure 7.15: Simulated voltage signal from reflection of an oscillating cathode wire with the bare signal without noise (left) and the FFT of this signal (right). The scale of the FFT magnitude is switched to a logarithmic scale above $200\,\mathrm{V}$.

The signal shown in figure 7.15 is superimposed with 10% noise, but is also shown once without it in order to better recognize the decay of the signal and the transient process. In this example, the FFT was performed after one second for a total of $2.5\,\mathrm{s}$. **The frequency determined using the "peak finder" exactly corresponds to the original signal frequency, as the peak visibly stands out in the spectrum.** Further simulations show that this is also the case whenever the signal is measured directly from the beginning. Therefore, in operation, the measurement can be carried out without delay after the wire has been deflected by the air blast.

This encourages the assumption that the WTTD, as has been described in this work, can perform its tasks more efficiently and precisely than its predecessors. Nevertheless, multiple measurements are required in order to exclude coincidental measurement uncertainties.

8 Conclusion and Outlook

The shape of the electric field and thus the amplification properties of a Multi Wire Proportional Chamber depend crucially on the uniform positioning of the electrode wires. Therefore, in the production process of the CBM TRD MWPCs, the wire-to-wire distance and their mechanical tension, preventing them from sagging in gravitational and electrical field, shall be examined precisely.
In order to be less invasive and time consuming this inspection shall be performed automatically and touchless by a Wire Tension Testing Device (WTTD).

The system consists of a measuring unit which can be positioned relative to the wire plane with a linear drive. The measurements themselves are conducted with an optical sensor that measures the reflection of light from the wires. To determine the tension of the wires, an oscillation is triggered by an air blast. The strength of the reflection subsequently oscillates and the mechanical tension can, thereby, be determined from the vibration frequency.
This thesis presents the basis for connecting the measurement components via a Controlled Area Network (CAN). Moreover, the software framework designed to control the components on the network through python scripts is implemented.

Furthermore, proposed core components for the system have been characterized. The linear drive (*HIWIN HM060S005*) was found to deliver sufficient positioning accuracy, as both the repeatability deviation and reversing play are in a range below $10\,\mu\mathrm{m}$. In addition, the thermal expansion of the spindle is negligible for moving speeds below $4\,{}^{\mathrm{cm}}/_{\mathrm{s}}$.
The motion controller, which controls the linear drive, can output the position synchronized with an effective sampling rate of up to $f_{\mathrm{N}} = 725\,\mathrm{Hz}$. Despite the fact that this last value is not completely satisfactory for tracking the position down to the smallest scale step even with fast movements, the combination of controller, drive and linear drive is suitable for the purposes of the WTTD.

The ADC (*MicroControl sensor module µCAN.1.ai-SENSOR / voltage*) that reads out the sensor should therefore also achieve at least this synchronization frequency during the scan of the wire position. However, the $f_\mathrm{N} = 400\,\mathrm{Hz}$ currently achieved are not sufficient for the desired data retrieval. Furthermore, the internal sampling of signals is only performed at a sampling rate of $f_\mathrm{s} = 40\,\mathrm{Hz}$. The expected frequencies for the tension measurement range up to $f_0 = 266\,\mathrm{Hz}$. In order to sample these correctly without interference of higher harmonics, a sampling rate and network frequency of at least $f_\mathrm{N} = f_\mathrm{s} = 1\,\mathrm{kHz}$ would be desirable.

Upon consultation with the manufacturer, the lack of performance could be attributed to a mismatch in the ADC product specifications. The delivery of a new, correspondingly faster sensor module is agreed and can be taken into operation in the commisioning setup created in this project. It is expected to have a sampling with up to $f_\mathrm{s} = 1\,\mathrm{kHz}$ available after this exchange, which would fit the WTTD requirements.

Also the currently selected sensor is not suitable, because it does not provide an analog voltage signal and the reflection is not focused enough to detect a single wire. Based on this recommendations for a suitable optical sensor could be given.

Furthermore, signal simulations have been conducted, resulting in the evolution of crucial analysis blocks. Together with the recommended component specifications, the measurement setup, control software and analysis routines implemented with the present work are expected to result in a capable, fast and precise measurement procedure.

Appendix A ALICE Field Simulations

In regard to the TRD modules used in the ALICE experiment at LHC some interesting simulations concerning the electric field and the wire sag were carried out and published in [Mah04]. Despite the fact that they relate to the geometry of the ALICE chambers, some important correlations can be identified. The simulations were carried out with the GARFIELD software. In the following simulation results, the unfavorable scenario of a direction of gravity that increases the electrostatic sag is always assumed [Mah04].

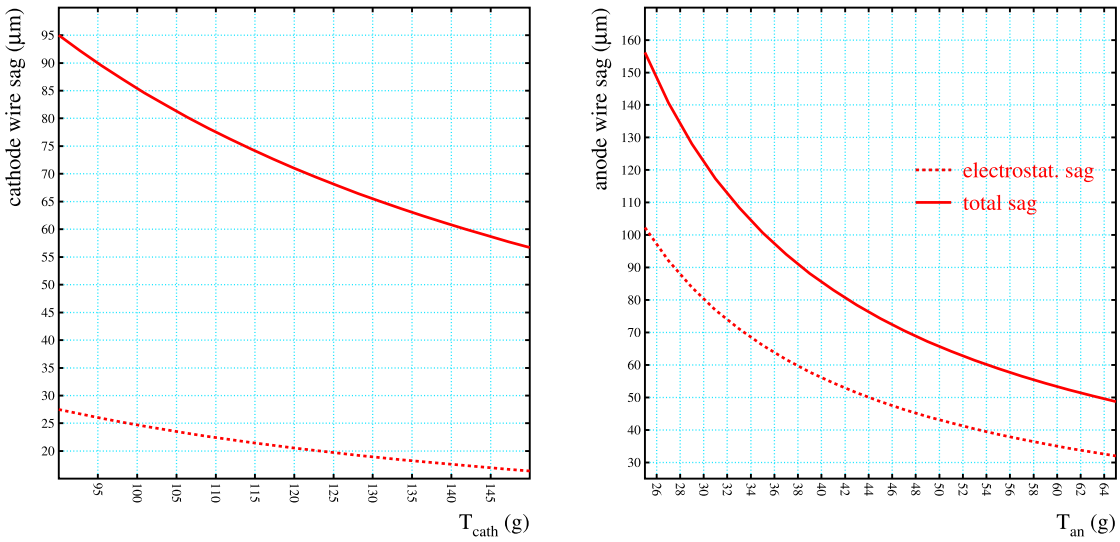

Figure A.1: Wire sag as a function of the wire tension for cathode (left) and anode (right) wires of the ALICE experiment [Mah04].

The simulations of the dependence of the wire sag on the tension result in graphs shown in figure A.1. Even with the interaction of gravitational and electrostatic components, the relationship for the electrostatic component as well as the total sag remains similar to $\Delta z \sim {}^{1}/_{T}$. The resulting force as the sum of the electrostatic and gravitational component can therefore still be described as acting per unit length $\mathrm{d}x$ according to equation (4.4).

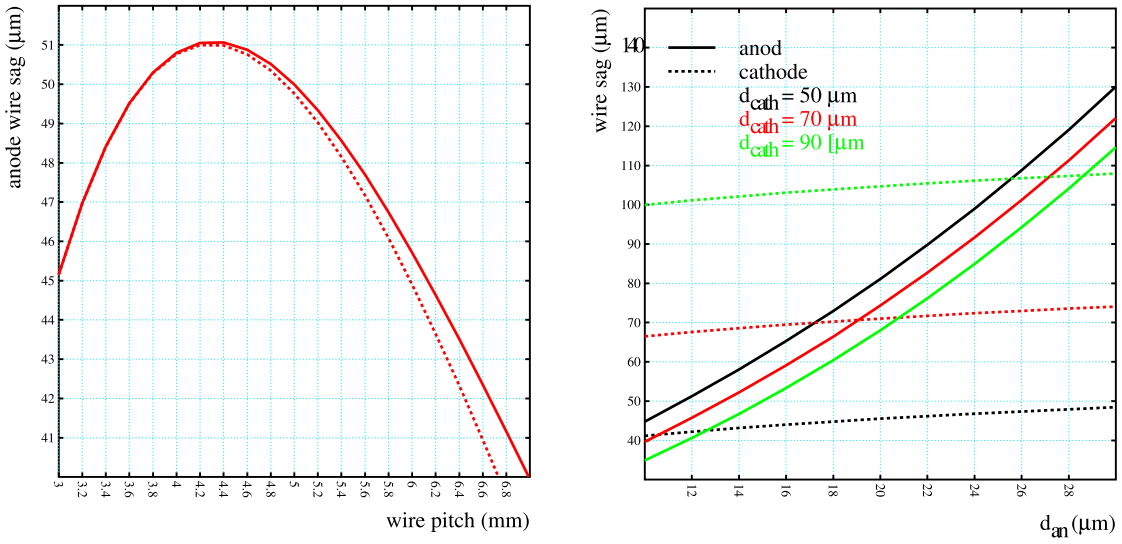

Figure A.2: Wire sag as a function of the anode wire pitch (left) and the wire diameter (right) [Mah04].

The pitch between the wire and the wire diameter are significant for the electric field. Therefore, the amplification properties as well as the wire sag caused by the electrostatic repulsion depend on it. Simulations for the latter are shown in figure A.2. Even though the electrostatic repulsion is getting smaller with rising pitch the wire sag first rises and then drops again for values of $d > 4.2\,\mathrm{mm}$. This is because to keep a wire at the same potential but with bigger pitch, the charge on it must be higher as well, leading to a greater attraction from the wires to the cathode planes. Also, the mirror charges in the pad plane are distributed onto a larger area with rising pitch, which decreases the attracting force from the cathodes again [Mah04]. The maximum in the wire sag shows, that these effects are dominant in different regions.

Looking at the right panel of figure A.2 it turns out, that the wire sag of the cathodes depends very little on the anode wire diameter because the electric field is almost homogeneous at the cathodes. However their wire sag does strongly depend on their own diameter due to the gravitational sag.

For the anode wires both components are important. Here the connection to the diameter is the surface pointing from one wire to another, where charges and mirror charges attract each other. The larger the surface gets the more charges participate in that.

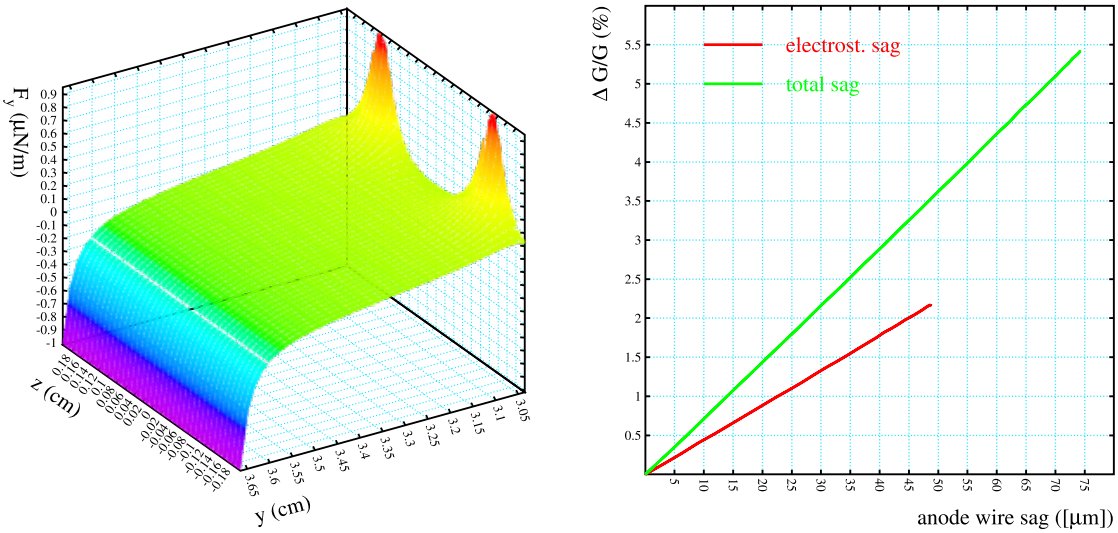

Figure A.3: Left: Elektrostatic component $f(z)$ acting on an anode wire as a function of its displacement (to be consistent with the coordinate system, the y- and z-directions must be swapped) [Mah04].
Right: Gain variation as a function of the wire sag.

The effect of a displaced anode wire on the force acting on it at a given wire pitch is displayed in figure A.3 on the left. Recognizable is the location of the adjoining wires, where the repelling force diverges. If the anode gets to close to the pad plane the electrostatic force is attracting. The conditions for this GARFIELD simulation is the nominal ALICE chamber geometry.

Further simulations show that the dependence of the gas gain on the wire sag is linear (figure A.3 right). At the smallest tolerable wire sags in the ALICE chambers of $\Delta z = 74\,\mu\mathrm{m}$ the relative gain variation is around 5.5%. Considering just the electrostatic force the wire sag as well as the gas gain variation would decrease.

Appendix B Wire Stress Strain Curve

In the following, a comprehensive examination of wire properties, including stress-strain characteristics, which have been derived from several testing procedures are presented. These analyses offer insights into the mechanical behavior and structural integrity of the wires. First, some definitions for the mechanical properties will be briefly reiterated.

Mechanical stress refers to the force exerted during deformation, represented by the tension T, per initial cross-sectional area A, whereas strain represents the ratio of total deformation to the initial dimensions of the material body subjected to external forces [MZ19]:

$$\text{Stress:} \quad \sigma = \frac{T}{A}, \qquad \text{Strain:} \quad \epsilon = \frac{l - l_0}{l_0}. \tag{B.1}$$

The tension T causes the body to deform from its initial length l_0 to a new length l. The stress-strain diagram depicting a rising tension on the wire is shown in figure B.1. This results in a progression that begins with a domain of elastic behavior. At this point the stress-strain curve is rising linear according to Hooke's law. The slope of this part $E = {}^{\Delta\sigma}/_{\Delta\epsilon}$ is called elastic modulus or Young's modulus [MZ19]. Young's modulus has the same unit as stress due to strain being dimensionless.

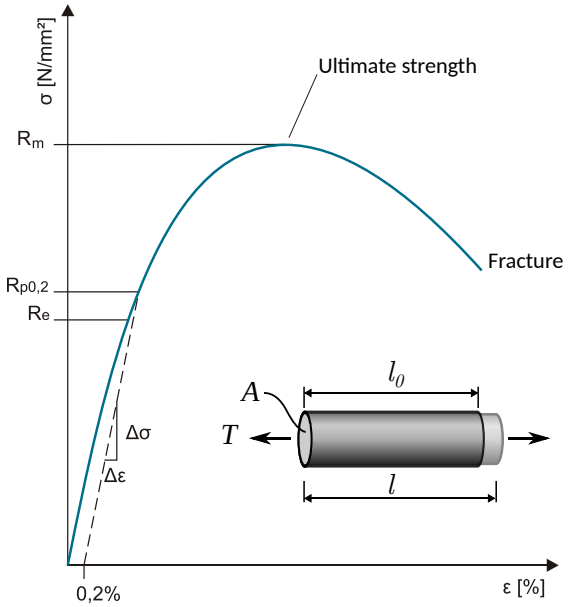

Figure B.1: Schematic stress-strain diagram with continuous start of yielding [Com21]. Modified from original.

Above a certain stress the deformation of the material is no longer elastic. That means that after applying the tension the material does not shrink back to its initial length l_0 again. The yield point R_e or yield strength is the stress limit of the elastic behavior. For certain materials, plastic deformation begins gradually, whereas for others, it is initiated locally, resulting in a jagged drop in the curve with a upper and lower yield point [MZ19]. Therefore, sometimes the offset yield point $R_{p0.2}$ is specified. This is the stress at which the permanent strain is $0.2\,\%$ after turning the stress off again [MZ19].

At even higher stress the material shrinks in its diameter. The maximum stress until a necking forms is called the tensile strength or ultimate tensile strength (UTS). In the stress-strain curve the shrinking cross section is not considered. Therefore the stress in figure B.1 decreases after this point while the tension T is still rising. The definition of the stress considering just the initial cross section is therefore often called engineer stress to distinguish it from "true stress". At even higher tension the material tears apart (fracture).

Table B.1: Properties of the Anode and cathode wires. Values written in black are from the GSI, while blue values are based on measurements from the manufacturer. The nominal values in red are taken from the data sheets.

	Anode		**Cathode**	
Manufacturer	Luma Metall AB		Elschukom GMBH	
Product number	LWWU861-020		101.017A.0075NO	
Production date	March 2022		June 2022	
Spool	165636		16062022102845	
Material	W + 3%Re +0.2 µm Au coating		Cu + 2%Be	
Diameter d in µm	20.1	20	75.5	75
Cross section A in mm^2	0.0003173		0.004477	
Density ρ in $\mathrm{g/cm^3}$	19.0	19.3	8.15	
Elastic modulus E in $\mathrm{kN/mm^2}$	376	430	≈ 100	
Yield point R_e in $\mathrm{N/mm^2}$	1639		-	
Offset yield point $R_{p0.2}$ in $\mathrm{N/mm^2}$	3000		1486	
Tensile strength R_m in $\mathrm{N/mm^2}$	3305	3700	1585	

For the wires used in the TRD stress-strain tests were carried out by the manufacturer as well as by J. Hehner and B. Fischer at the GSI. The values that were achieved are shown in table B.1.

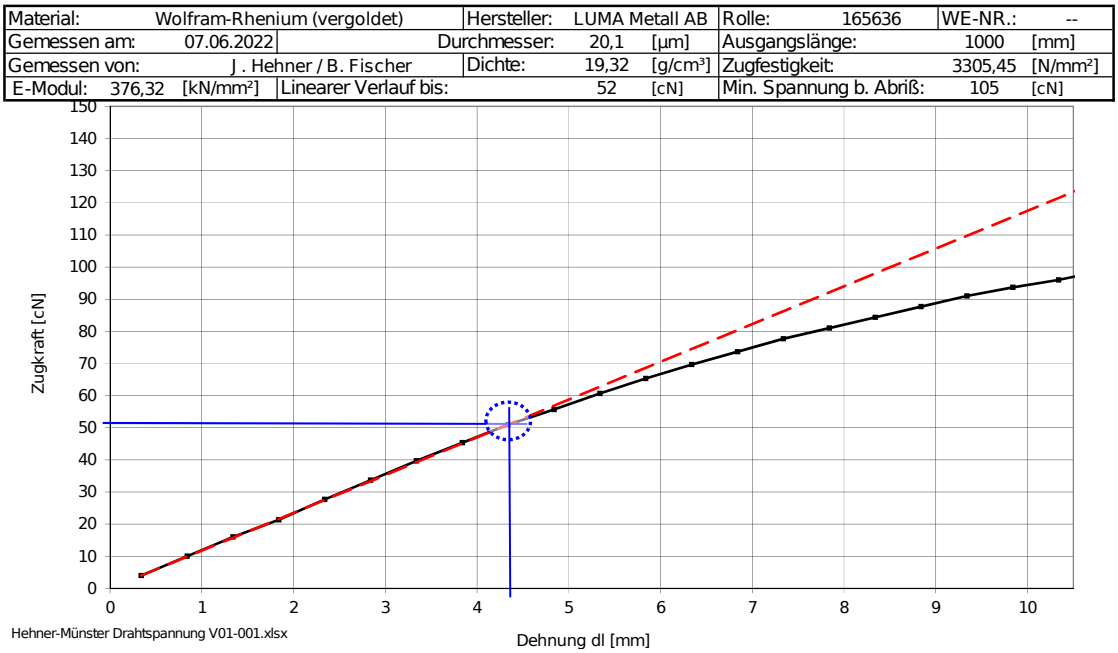

Figure B.2: Stress-strain curve based on a measurement of the anode wires carried out at GSI. It depicts the yield point (blue) at which the data (black) no longer rises linear.

During the GSI measurement, three wires with a initial length of $l_0 = 100\,\mathrm{cm}$ were stressed until they tore apart. The data was averaged and a linear fit was performed using the first data points in order to determine the elastic modulus and the yield point. Figure B.2 shows the section of the measured stress strain curve around the yield point.
The wire has a continuous yield, as the data points increase monotonically. The cross section was determined using an optical microscope (Keyence VHX x1500).

Appendix C Analysis and Simulation Scripts

For the determination of the wire tension the spectrum of the reflection signal is calculated and the fundamental frequencie is determined using a peakfinder algorhitm. This code implementation is shown in listing C.1.

```
def FFT(time0, voltage0, window=(0,1),expected_freq=None,
   height=None, threshold=None, distance=None, prominence=
   None, width=None, wlen=None, rel_height=0.5,
   plateau_size=None):
    # Implementation of the time window
    start_index,end_index  = int(len(time0) * window[0]),
       int(len(time0) * window[1])-1
    if time0[end_index]-time0[start_index] <= 2.5: # If
       the time window is too small the resolution of the
       FFT frequencies is not sufficient to calculate the
       Tension within a 1% deviation
        print('Window is to small to get sufficient
           frequency resolution.')
    time, voltage = time0[start_index:end_index], voltage0
       [start_index:end_index]

    # Compute FFT and frequencies
    fft_magn, fft_freq = np.abs(fft(voltage)), fftfreq(len
       (voltage), time[1] - time[0])

    # Implementation of the expected frequency. In a +-10%
        range around it the fundamental frequency is been
       searched for
    if expected_freq == None:
        f_lo,f_up = min(fft_freq), max(fft_freq)
    else:
        f_lo,f_up = 0.9*expected_freq, 1.1*expected_freq

    # Find peaks in the FFT magnitude
    peaks, _ = find_peaks(fft_magn[(fft_freq>=f_lo) & (
       fft_freq <= f_up)], height, threshold, distance,
       prominence, width, wlen, rel_height, plateau_size)
```

```
    # Find the first peak (excluding DC component)
    if len(peaks) > 1:
        fundamental_peak = next((peak for peak in peaks if
            fft_freq[(fft_freq>=f_lo) & (fft_freq <= f_up)
           ][peak] > 0), None) # Exclude the DC Component
           @0Hz
        fundamental_freq = fft_freq[fundamental_peak]
    # if no peaks meet the requirements given as
       parameters in findpeaks the frequency with the
       highest magnitude is chosen
    else:
        fundamental_freq = fft_freq[(fft_freq>f_lo) & (
           fft_freq <= f_up)][np.argmax(fft_magn[(fft_freq
           >f_lo) & (fft_freq <= f_up)])]

    return fft_magn, fft_freq, u.ufloat(fundamental_freq,
       np.diff(fft_freq).max())
```

Listing C.1: Python function to calculate the frequency spectrum and the fundamental frequency.

In order to test this function without real data the signal of an oscillating wire is simulated with the code given in listing C.2.

```
def sim_signal(frequency, samplingrate=400, duration=10,
   amplitude=1, phase=0, noise_ratio=0.1, decay_cons=0.2,
   offset=0, transient_duration=0.1):
    time = np.arange(0, duration, 1/samplingrate)

    # Generate transient oscillation signal
    transient_time = time[time<duration*transient_duration
       ]
    transient_amplitude = np.linspace(0, amplitude, len(
       transient_time))               # Rising amplitude
       of the transient oscillation
    transient_oscillation = np.zeros_like(
       transient_amplitude)
```

```
    for irregularitiy in range(10):

        # Add a transient oscilation as superimposed random
         irregularities
         irregular_frequency = frequency*10 * np.random.
            rand()                                  # Random
            frequency below the target frequency
         irregular_amplitude = np.random.rand()*amplitude
                                            # Random
            amplitude below the target amplitude
         transient_oscillation += transient_amplitude *
            irregular_amplitude * np.sin(2 * np.pi *
            irregular_frequency * transient_time)
    transient_oscillation *= amplitude / np.max(np.abs(
        transient_oscillation)) if np.max(np.abs(
        transient_oscillation)) > amplitude else 1 #rescale
         signal to amplitude

    # Generate main oscillation signal
    main_time = time[time>=duration*transient_duration]
    main_oscillation = amplitude * np.sin(2 * np.pi *
        frequency * main_time + phase)
    # Add higher harmonics
    for harmonic in range(2, min(5, (samplingrate//2) //
        frequency) + 1):                    # Add harmonics
        until harmonic * frequency exceeds half the
        samplingrate to prevent undersampling but add 5
        harmonics max
         harmonic_frequency = frequency * harmonic
                                                    #
            frequency of higher harmonics is always a
            multiple of the fundamental frequency
         harmonic_amplitude = amplitude / harmonic
                                                    #
            Adjust amplitude for each harmonic
         main_oscillation += harmonic_amplitude * np.sin(2
            * np.pi * harmonic_frequency * main_time) # add
             the higher harmonics to the signal
```

```
    main_oscillation *= amplitude / np.max(np.abs(
        main_oscillation)) if np.max(np.abs(
        main_oscillation)) > amplitude else 1 #rescale
        signal to amplitude

    # Concatenate transient and main signals
    oscillation = np.concatenate((transient_oscillation,
        main_oscillation))
    noise = np.random.normal(loc=0, scale=noise_ratio *
        amplitude, size=len(time))
    decay = np.exp(-decay_cons * time)

    signal = decay * oscillation + noise + offset
    return time, signal
```

Listing C.2: Python function to simulate the signal of an oscillating wire.

Appendix D Uncertainty Treatment

In regard to the specification and handling of calculations with uncertainties in measurement variables, the guidelines of the "Guide to the Expression of Uncertainty in Measurement" [GUM20] was applied.
Unless otherwise specified, the uncertainty of digital values d (MC position/increments, temperature, etc.) results from the rectangular distribution of the smallest displayable digit Δd:

$$\sigma_d = \frac{\Delta d}{2\sqrt{3}}.$$

For analoge values a (the dial gauge in particular) the uncertainty on the other hand is given by a triangular distribution from the smallest scale increment Δa:

$$\sigma_a = \frac{\Delta a}{2\sqrt{6}}.$$

If a mean value is calculated from values that all have the same uncertainty, the total uncertainty is obtained by directly propagating the individual uncertainty and the standard deviation from the mean value. The direct propagation of several uncertainties σ_i is thereby given as:

$$\sigma = \sqrt{\sum_{i=1}^{N} \sigma_i^2}.$$

If the values for the average have different uncertainties, this is replaced by a fit using a constant, performed with scipy.odr in python (least squares method), which weights the individual uncertainties with the total deviation from the fit.
For a quantity X that is depending on several quantities x_i that all have an uncertainty σ_{x_i} the indirect propagation of uncertainties according to the Gaussian uncertainty propagation formula:

$$\sigma_X = \sqrt{\sum_{i=1}^{N} \left(\frac{\partial X}{\partial x_i}\right)^2 \sigma_{x_i}^2}$$

is used. In particular this is done for equation (4.20) calculating the wire tension from the fundamental frequency in section 7.2.2.

Bibliography

[Apr23] V. Aprodu et al. *Addendum TRD TDR: An Enhanced Tracking Device For the Inner Region of the TRD wall*. Tech. rep. CBM Collaboration, Feb. 2023.

[ASM02] F. Cverna and ASM International. Materials Properties Database Committee. *ASM Ready Reference: Thermal properties of metals*. ASM Ready Reference Series. ASM International, 2002. ISBN: 978-0871707680.

[AW12] A. Andronic and J.P. Wessels. "Transition radiation detectors". In: *Nuclear Instruments and Methods in Physics Research Section A: Accelerators, Spectrometers, Detectors and Associated Equipment* 666 (Feb. 2012), pp. 130–147. ISSN: 0168-9002. DOI: 10.1016/j.nima.2011.09.041.

[BR08] W. Blum and L. Rolandi. *Particle detection with drift chambers*. 2ed. Particle Acceleration and Detection. Springer Berlin Heidelberg, 2008. ISBN: 978-3-540-76683-4. DOI: 10.1007/978-3-540-76684-1.

[Com21] Wikimedia Commons. *File:Spgs-Dehnungs-Kurve Dehngrenze.svg — Wikimedia Commons, the free media repository*. 2021. URL: https://commons.wikimedia.org/wiki/File:Spgs-Dehnungs-Kurve_Dehngrenze.svg (visited on 03/26/2024).

[DF03] A. Das and T. Ferbel. *Introduction to Nuclear and Particle Physics*. EBSCO ebook academic collection. World Scientific, 2003. ISBN: 978-981-256-435-1.

[Ers72] G.A. Erskine. "Electrostatic problems in multiwire proportional chambers". In: *Nuclear Instruments and Methods* 105.3 (1972), pp. 565–572. ISSN: 0029-554X. DOI: 10.1016/0029-554X(72)90356-4.

[Ese18] M. Esen. "Implementation of an Automated Position and Tension Determination of Wires in Multi-Wire Proportional Chambers". Goethe- Universität Frankfurt am Main, Institut für Kernphysik, Nov. 2018.

[Fal22] M. Falch. *CANopen Explained - A Simple Intro*. CSS Electronics. 2022. URL: https://www.csselectronics.com/pages/canopen-tutorial-simple-intro (visited on 04/02/2024).

[Fri11] B. Friman et al., eds. *The CBM physics book: Compressed baryonic matter in laboratory experiments*. Vol. 814. Lecture Notes in Physics. 2011, pp. 1–980. DOI: 10.1007/978-3-642-13293-3.

[Got05] H. Gottschlag. "Entwicklung einer Apparatur zur automatisierten Positions- und Spannungsbestimmung von Drähten in Vieldrahtproportionalkammern". Universität Münster, Institut für Kernphysik, Feb. 2005.

[Gre00] D. Green. *The Physics of Particle Detectors*. Vol. 12. Cambridge Monographs on Particle Physics, Nuclear Physics and Cosmology. Cambridge University Press, 2000. ISBN: 978-0521662260.

[Gru93] C. Grupen. *Teilchendetektoren*. BI-Wiss.-Verlag, 1993. ISBN: 978-341-116-571-1.

[GUM20] BIPM et al. *Guide to the expression of uncertainty in measurement — Part 6: Developing and using measurement models*. Joint Committee for Guides in Metrology, JCGM GUM-6:2020. 2020. URL: https://www.bipm.org/utils/common/documents/jcgm/JCGM_GUM_6_2020.pdf.

[Gut06] H. Gutbrod et al. *FAIR-Baseline technical report. Executive summary*. Darmstadt: GSI, 2006. ISBN: ISBN 978-3-9811298-0-9.

[KW16] H. Kolanoski and N. Wermes. *Teilchendetektoren: Grundlagen und Anwendungen*. Springer, 2016. ISBN: 978-3-662-45350-6. DOI: 10.1007/978-3-662-45350-6.

[LSM16] S.J. Ling, J. Sanny, and W. Moebs. *University Physics*. Online access: Center for Open Education Open Textbook Library Bd. 1. OpenStax, Rice University, 2016. ISBN: 978-1938168277.

[Mah04] T. Mahmoud. "Development of the Readout Chamber of the ALICE Transition Radiator Detector and Evaluation of its Physics Performance in the Quarkonium Sector". PhD thesis. Ruperto-Carola University of Heidelberg, Combined Faculties of Natural Sciences and Mathematics, May 2004.

[Mat88] E. Mathieson. "Cathode charge distributions in multiwire chambers: 4. Empirical formula for small anode-cathode separation". In: *Nuclear Instruments and Methods in Physics Research Section A: Accelerators, Spectrometers, Detectors and Associated Equipment* 270.2 (1988), pp. 602 –603. DOI: 10.1016/0168-9002(88)90736-X.

[MF53] P.M. Morse and H. Feshbach. "Solutions of Laplace's and Poisson's Equations". In: *Methods of Theoretical Physics*. International Series in Pure and Applied Physics. McGraw-Hill, 1953. Chap. 10. ISBN: 978-0-0704331-7-5.

[Micro] MicroControl. *µCAN.sensor Manual Analogue Data Acquisition for OEM-customers*. Version 1.02. MicroControl GmbH & Co. KG. Troisdorf.

[MZ19] E. Macherauch and H.W. Zoch. *Praktikum in Werkstoffkunde: 100 ausführliche Versuche aus wichtigen Gebieten der Werkstofftechnik*. Springer Fachmedien Wiesbaden, 2019. ISBN: 978-3-658-25374-5. DOI: 10.1007/978-3-658-25374-5_22.

[PAK08] O. Pfeiffer, A. Ayre, and C. Keydel. *Embedded Networking with CAN and CANopen*. Copperhill Technologies Corporation, 2008. ISBN: 978-0-9765116-2-5.

[PK20] A. Puntke and P. Kähler. "Position Reconstruction in DESY 2017 Testbeam Data". In: *CBM Progress Report 2019*. GSI Helmholtzzentrum für Schwerionenforschung GmbH, Darmstadt, Germany, 2020. ISBN: 978-3-9815227-8-5. DOI: 10.15120/GSI-2020-00904.

[Pre07] W. Press et al. "Fast Fourier Transform". In: *Numerical Recipes: The Art of Scientific Computing*. Cambridge, UK: Cambridge Univ. Press, 2007. Chap. 12.

[Sch05] M. Schleicher. *Digitale Schnittstellen und Bussysteme: Grundlagen und praktische Hinweise zur Anbindung*. Messen - regeln - registrieren. JUMO, 2005. ISBN: 9783935742023.

[TDR18] C. Blume et al. *The Transition Radiation Detector of the CBM Experiment at FAIR: Technical Design Report for the CBM Transition Radiation Detector (TRD)*. Tech. rep. Collaboration FAIR: CBM, 2018. DOI: 10.15120/GSI-2018-01091.

[Tek12] Tektronix, Inc. *AFG3021 in AFG3000 Series Arbitrary-Function Generators Datasheet*. Beaverton, OR 97077, July 2012.

[Tho13] M. Thomson. *Modern Particle Physics*. Modern Particle Physics. Cambridge University Press, 2013. ISBN: 978-1107034266.

Acknowledgements

Finally, I would like to take this opportunity to thank everyone who has contributed to the success of this work and supported me.
First and foremost, I would like to thank my professors and supervisors Anton Andronic and Christian Klein-Bösing. You gave me a great opportunity to be involved in research for the first time. I was able to discover and learn a lot of new things during this time and I am very happy that my time as a bachelor student is coming to an end in this way.
I would like to thank Philipp Kähler for his help with my work both in the lab, on the text and by patiently answering my questions. Without you, I would have made much less progress.
Thanks also go to Daniel Bonaventura, who assembled the setup, helped me with the soldering and also created the CAD render of the WTTD given in this thesis.
I owe the greatest progress at the beginning of my work to Liridon Deda, who gave me a first short code snippet for the control of CAN with Python.
Special thanks go to my office colleagues. I would like to thank Philipp for his help with my numerous computer problems, Luisa for motivation, help with writing and many quick answers, Axel for tips on programming and many other questions, Felix for useful hints and his great helpfulness also in the lab and Adrian for answers on the physical background and the CBM detectors.
I would also like to thank the entire working group for the great time and the warmth with which I was welcomed and treated for the whole time. Each of you was super helpful and encouraged me in various ways. All of you have become very dear to me and I will look back fondly on my time with you.